Published in final edited form as:
Vis Neurosci. 2014 January ; 31(1): 57–84. doi:10.1017/S0952523813000461.

A synaptic signature for ON- and OFF-center parasol ganglion cells of the primate retina

Joanna D. Crook, **Orin S. Packer**, and **Dennis M. Dacey**
Department of Biological Structure, University of Washington and the Washington National Primate Research Center (NPRC), Seattle, Washington

Abstract

In the primate retina, parasol ganglion cells contribute to the primary visual pathway *via* the magnocellular division of the lateral geniculate nucleus, display ON and OFF concentric receptive field structure, nonlinear spatial summation, and high achromatic temporal–contrast sensitivity. Parasol cells may be homologous to the alpha-Y cells of nonprimate mammals where evidence suggests that N-methyl-D-aspartate (NMDA) receptor-mediated synaptic excitation as well as glycinergic disinhibition play critical roles in contrast sensitivity, acting asymmetrically in OFF- but not ON-pathways. Here, light-evoked synaptic currents were recorded in the macaque monkey retina *in vitro* to examine the circuitry underlying parasol cell receptive field properties. Synaptic excitation in both ON and OFF types was mediated by NMDA as well as α-amino-3-hydroxy-5-methyl-4-isoxazolepropionic acid (AMPA)/kainate glutamate receptors. The NMDA-mediated current–voltage relationship suggested high Mg^{2+} affinity such that at physiological potentials, NMDA receptors contributed ~20% of the total excitatory conductance evoked by moderate stimulus contrasts and temporal frequencies. Postsynaptic inhibition in both ON and OFF cells was dominated by a large glycinergic “crossover” conductance, with a relatively small contribution from GABAergic feedforward inhibition. However, crossover inhibition was largely rectified, greatly diminished at low stimulus contrasts, and did not contribute, *via* disinhibition, to contrast sensitivity. In addition, attenuation of GABAergic and glycinergic synaptic inhibition left center–surround and Y-type receptive field structure and high temporal sensitivity fundamentally intact and clearly derived from modulation of excitatory bipolar cell output. Thus, the characteristic spatial and temporal–contrast sensitivity of the primate parasol cell arises presynaptically and is governed primarily by modulation of the large AMPA/kainate receptor-mediated excitatory conductance. Moreover, the negative feedback responsible for the receptive field surround must derive from a nonGABAergic mechanism.

Keywords

Magnocellular pathway; NMDA receptor; Glycine receptor; Excitation; Inhibition

---

Address correspondence to: Dennis M. Dacey, Department of Biological Structure, University of Washington, Seattle, WA 98195. dmd@uw.edu.

Introduction

In the visual pathway of primates, the magnocellular division of the lateral geniculate nucleus (LGN) relays an achromatic signal with high temporal and contrast sensitivity to primary visual cortex (Derrington & Lennie, 1984; Callaway, 2005; Lennie & Movshon, 2005). One major, and well identified, retinal ganglion cell type that projects to the magnocellular LGN, the parasol cell (Leventhal et al., 1981; Perry et al., 1984; Dacey et al., 2003), has been the focus of intensive physiological (Lee et al., 1988; Kaplan et al., 1990; Kaplan & Benardete, 2001; Field & Chichilnisky, 2007) and anatomical investigation (Watanabe & Rodieck, 1989; Dacey & Petersen, 1992; Silveira et al., 2004; Lee et al., 2010). Parasol cells form anatomically distinct ON- and OFF-center populations, show concentric center–surround receptive field structure, and share many properties with the alpha ganglion cell type of cats and other mammals (Watanabe & Rodieck, 1989; Peichl, 1991; Dacey & Brace, 1992), including nonlinear spatial summation (Crook et al., 2008*b*).

Application of the voltage clamp to identify light-evoked excitatory and inhibitory synaptic conductances in alpha-Y cells suggests unanticipated circuit elements that underlie critical features of the light response. In guinea pig retina, N-methyl-D-aspartate (NMDA)-type glutamate receptors have been implicated in contributing to contrast sensitivity near threshold in OFF- but *not* ON-center alpha-Y cells (Manookin et al., 2010). In addition, a similar NMDA receptor-mediated component of the light response of other nonalpha ganglion cell types in rabbit retina has been recently described (Venkataramani & Taylor, 2010; Buldyrev et al., 2012; Buldyrev & Taylor, 2013). The picture that emerges from these studies is that NMDA receptors may contribute differentially to diverse ganglion cell types and to OFF *versus* ON pathways. An NMDA receptor contribution to the light-evoked spike discharge of primate ganglion cells has been described (Cohen & Miller, 1994), and preliminary evidence for a large NMDA receptor contribution to the primate midget ganglion cell pathway has been observed (Crook et al., 2011). However a role for, or even the specific presence of, NMDA receptor-mediated excitation in ON and/or OFF parasol cells has not been determined. One major goal of the present study therefore was to isolate and characterize any NMDA receptor-mediated synaptic conductance in both ON and OFF parasol ganglion cells.

Similarly, again in OFF alpha cells, a glycinergic inhibitory conductance in antiphase to synaptic excitation, often referred to as “crossover” inhibition (Werblin, 2010) has been identified (Murphy & Rieke, 2006; van Wyk et al., 2009) and shown to act, *via* disinhibition, to increase contrast sensitivity at threshold (Manookin et al., 2008). In primate retina, it is striking that glycinergic crossover inhibition is observed in parasol and small bistratified blue-ON but not midget ganglion cells (Crook et al., 2009*b*; Cafaro & Rieke, 2013; Crook et al., 2013; Dacey et al., in press). Thus, a second goal of this study was to determine whether crossover inhibition in parasol ganglion cells contributes *via* disinhibition to the high temporal–contrast sensitivity in OFF and/or ON parasol cells.

In rabbit, the alpha-Y cell receptive field surround appears to arise largely postsynaptically, by amacrine cell-mediated lateral inhibition (Taylor, 1999; Flores-Herr et al., 2001). By contrast, there is evidence that the surround of both midget and parasol cells arises mostly presynaptically, *via* excitatory input from cone bipolar cells with well developed center–surround organization (Dacey et al., 2000; McMahon et al., 2004; Crook et al., 2011). Moreover, the creation of this surround *via* horizontal cell negative feedback to cone photoreceptors appears to utilize a novel mechanism (Fahrenfort et al., 2009; Thoreson & Mangel, 2012) that does not require synaptic inhibition (McMahon et al., 2004; Davenport et al., 2008; Crook et al., 2011). The nonlinear spatial structure of the alpha-Y cell receptive field has also been proposed to arise either by synaptic inhibition (Hochstein & Shapley, 1976; Victor & Shapley, 1979; Frishman & Linsenmeier, 1982) or *via* postsynaptic summation of excitatory input from transient cone bipolar cells (Demb et al., 2001; Crook et al., 2008*b*). Recently, it has been suggested that crossover inhibition in ON parasol cells shapes the timing of the Y-type light response (Cafaro & Rieke, 2013). Thus, a final goal of this study was to determine the degree to which postsynaptic inhibition contributes to center–surround and Y-type nonlinear receptive field structure.

To begin to address these diverse questions, we used the voltage clamp to characterize the excitatory and inhibitory synaptic conductances evoked in parasol cells by a variety of spatio-temporal visual stimuli. We found that for both ON and OFF types postsynaptic excitatory currents were mediated by NMDA as well as α-amino-3-hydroxy-5-methyl-4-isoxazolepropionic acid (AMPA)/kainate glutamate receptors. However, the NMDA receptor-mediated currents made a relatively small contribution to the total light-evoked conductance across a range of stimulus contrasts and thus did not appear critical for driving the characteristic contrast gain of parasol cells. Postsynaptic inhibition in both ON- and OFF-center parasol types was dominated by a glycinergic crossover conductance. However, this inhibitory conductance was largely rectified and greatly diminished at low stimulus contrasts and thus did not contribute *via* disinhibition to contrast sensitivity in parasol cells. Finally, both center–surround receptive field structure and nonlinear spatial summation were derived from modulation of postsynaptic excitation and were largely unaltered by attenuation of synaptic inhibition with GABAergic and/or glycinergic receptor antagonists. Overall our results suggest that the fundamental physiological properties of parasol ganglion cells are established largely by modulation of the excitatory bipolar output acting largely at nonNMDA glutamate receptors.

Materials and methods

In vitro retinal preparation

Basic protocols for preparing the macaque retina–retinal pigment epithelial (rpe)–choroid for *in vitro* maintenance have been described previously (Crook et al., 2009*a*; Crook et al., 2011). In brief, eyes from either of two species of macaque monkey (*M. nemestrina, M. fascicularis*) were acquired in full room lighting conditions, after euthanasia, from the Tissue Distribution Program of the National Primate Research Center following protocols in accordance with the Institutional Animal Care and Use Committee at the University of Washington. After enucleation, the cornea was removed from the globe by a vertical razor cut at the limbus, and the vitreous body was removed. The retina, together with the choroid and rpe layers, was then placed in oxygenated Ames medium and dissected from the sclera, again at photopic light levels. After dissection, the retina–choroid–rpe was adhered to the glass bottom of a stainless steel superfusion chamber coated with poly-L-lysine (0.1%) and equipped for temperature regulation. The retina was adhered to the chamber bottom with the thick and fenestrated choroid side down and the inner retinal surface up to facilitate easy visualization and targeting of ganglion cell types under microscopic control. The chamber was mounted on the stage of a light microscope; oxygenated bicarbonate buffered Ames culture medium (pH 7.3; Sigma or American Biological) superfused the retina at a rate of ~5 ml/min, maintained at a temperature of ~36 deg. Once the retina was fixed to the microscope stage, it was maintained throughout the experiment in a light-adapted state by ambient room lighting around the recording setup. Experiments were usually terminated after ~36 h as a precaution against any changes in retinal circuitry or function as a result of extended periods *in vitro*.

The ganglion cell layer was observed with differential interference optics under near infrared illumination. Both ON- and OFF-center parasol ganglion cells could be reliably distinguished by large soma diameters relative to other ganglion cell types, and cell type identity was confirmed by either direct observation of dendritic morphology observed episcopically by fluorescent dye (Alexa Fluor 488, 50–100 μM, A10436, Invitrogen, Carlsbad, CA) injection during intracellular recording or by a characteristic receptive field center diameter in near peripheral retina as well as a noncolor opponent light response relative to other ganglion cell types (Crook et al., 2008*b*).

In vitro electrophysiology

Basic patch recording methods have been published previously (Crook et al., 2011). In brief, patch pipettes made from borosilicate glass were filled with either Ames medium for extracellular “loose” patch recordings or with a cesium-based solution for intracellular measurement of light-evoked whole-cell synaptic currents. The filling solution contained (in millimolar): 120 cesium-methanesulfonate, 5 tetraethylammonium (TEA)-Cl, 10 Hepes, 3 NaCl, 10 Bapta, 2 lidocaine *N-ethyl* bromide (QX-314), 2 ATP-Mg, and 0.3 GTP-Na adjusted to pH 7.3. Cesium replaced potassium to reduce voltage-gated potassium currents. QX-314 blocked voltage-gated sodium channels and eliminated spike discharge after establishing the whole-cell configuration. The chloride reversal potential calculated for this internal solution was—65 mV and this value was used for the conductance analysis as described below. In making this calculation, we assumed that bromide (2 mM) was 1.5 times more permeable than chloride for the GABA and glycinegated channels (Bormann et al., 1987). We calculated the liquid junction potential to be 12.63 mV and therefore subtracted 13 mV from all command voltages.

All signals were acquired at a 10 kHz sample rate and filtered (at 2 kHz or 5 kHz) with an AxoClamp 200B amplifier (Molecular Devices, Sunnyvale, CA) and a Heka InstruTECH ITC-1600 Data Acquisition Interface. Generation and presentation of light stimuli and display and storage of all membrane currents were controlled by custom software described in detail elsewhere (http://vrc.biostr.washington.edu/vct/vct_home.html) and made freely available to the research community.

After establishing the whole-cell configuration parasol cells in which synaptic currents could be measured successfully over an extended time period typically displayed whole-cell capacitances of ~ 50 to 70 pF ($n = 21$; mean ± S.D. = 67 ± 8), input resistances of ~ 50 to 75 M Ω ($n = 21$; mean ± S.D. = 61 ± 25), access (series) resistances of ~12 MΩ ($n = 35$; mean ± S.D. = 13 ± 3), and the zero current potential stabilized at approximately −40 mV ($n = 21$; mean ± S.D. = −38 ± 8). Stimulus-evoked synaptic currents were acquired from parasol cells over a series of holding potential steps ranging from approximately −100 mV to +25 mV (after subtraction of junction potential) at approximately 15 mV increments. Because parasol cells can show relatively large synaptic currents, we needed to correct for the potentially large errors in actual membrane holding potential, relative to the command potential, introduced by these large ionic currents across the series resistance introduced by the recording pipette. We therefore first used the series resistance compensation circuitry of the AxoClamp amplifier (prediction and correction used sequentially and carefully following the instructions in the Theory and Operation manual provided by the original manufacturer) to achieve ~95% series resistance and whole cell capacitance compensation during the recording and before light-evoked currents were collected. This correction was checked after each voltage step-light stimulus family was acquired, typically once per minute and adjustments in the correction were made if the series resistance changed during a typical 20- to 60-min recording period. For the majority of cells used in this study, series resistance values tended to vary between 10 and 20 M Ω during a recording period. The recorded series resistance was also used to correct for the small residual uncompensated series resistance (Crook et al., 2011). The final corrected holding potential at each time point was given by: $V_{\text{hold}}(t) = V_{\text{command}} - (I_{\text{measured}}(t) \times R_{\text{s}} \times (1 - R_{\text{scorrect}}))$, where V_{command} is the command potential—the 13-mV junction potential. I_{measured}, the current (nA) measured at each time point of stimulus presentation, is equivalent to the sum of a constant current (nA) measured after the holding potential step 50 ms prior to stimulus onset and the time varying stimulus-evoked current. R_{s} is the series resistance (MΩ) measured with the AxoClamp resistance compensation circuit before stimulus onset and R_{scorrect} is the series resistance compensation (typically 0.95 was reliably achieved when R_{s} was between 10–15 MΩ). It is worth noting that even at time points with very large light-evoked currents ~2 nA recorded in parasol ganglion cells, with 90% compensation (assuming ~15 MΩ R_{s}), the V_{hold} error correction would only be ~3 mV.

These corrected V_{hold} families were used to plot the current– voltage (I–V) relationship over the time course of the stimulus at 1.5-ms intervals during the light-evoked synaptic current. Even in cases where the overall I–V relationship was relatively linear, there were variable deviations at the extreme positive and negative holding potentials. Thus, to estimate the contribution of a linear synaptic excitation ($E_{\text{cat}} = 0$ mV) and inhibition ($E_{\text{Cl}} = -65$ mV) to the total conductance, we fit the I–V relationship for each plot using the four holding potential values on either side of the reversal or zero current potential (e.g., Fig. 1). This had little effect on the calculated reversal potentials but on average slightly reduced the calculated value of the inhibitory relative to the excitatory conductances.

We used these data to model the total conductance as the sum of a linear excitatory conductance with a reversal potential (E_{cat}) of 0 mV and a linear inhibitory conductance of −65 mV taken from our calculated E_{Cl}, following methods described previously (Borg-Graham, 2001; Taylor & Vaney, 2002; Crook et al., 2011). Briefly, the linear fit to the I–V

relationship is a straight line, $I(V) = G_{\text{total}} \times V + I_{\text{intercept}}$, with a slope equal to total conductance, G_{total}, that crosses the V axis at the reversal potential, $V_{\text{rp}} = -I_{\text{intercep}}/G_{\text{total}}$. The excitatory component of the I–V relationship is modeled as a straight line of the slope $G_{\text{cation}} = G_{\text{tot}} \times (V_{\text{rp}} - E_{\text{Cl}})/(E_{\text{cation}} - E_{\text{Cl}})$ with a reversal potential of E_{cation}. The inhibitory component of the I–V relationship is modeled as a straight line of slope $G_{\text{Cl}} = G_{\text{total}} \times (V_{\text{rp}} - E_{\text{cation}})/(E_{\text{Cl}} - E_{\text{cation}})$ with a reversal potential of E_{Cl}.

This analysis makes the assumption that the I–V relationship is reasonably well fit by a straight line. However, as will be demonstrated in the Results and is common for the light-evoked synaptic currents of many ganglion cell types (Mittman et al., 1990; Cohen, 1998, 2000; Manookin et al., 2008; Venkataramani & Taylor, 2010; Crook et al., 2011; Buldyrev et al., 2012), a voltage-dependent NMDA-type glutamate receptor contributes a nonlinear excitatory conductance to the I–V plot. The negative slope conductance at negative holding potentials sums with the linear component contributed by AMPA/kainate receptors and reduces the current values from about −100 to −40 mV. To estimate the magnitude and time course of the separate nonlinear NMDA, linear nonNMDA, and inhibitory conductances, we fit the synaptic I–V relationship with an equation (Buldyrev et al., 2012) that describes the NMDA current as a function of voltage:

$$I(V)=G_{\text{Cl}}(V-E_{\text{Cl}})+(G_{\text{cation}}+G_{\text{NMDA}}\times f(V))(V-E_{\text{cation}}), \quad (1)$$

where $f(V)$ is the fraction of NMDA channels that are conducting at voltage V

$$f(V)=1-([\text{Mg}]/([\text{Mg}]+K_{\text{Mg}}\times \text{e}^{(V/V)}\delta)). \quad (2)$$

E_{Cl} (mV) is the inhibitory chloride reversal potential, E_{cation} (mV) is the excitatory cation reversal potential, [Mg] (mM) is the extracellular magnesium (Mg) concentration (1.2 mM), K_{Mg} (mM) is the apparent Mg binding affinity at 0 mV, and V_{δ} (mV) is proportional to the fraction of the membrane electric field sensed by the Mg ion at the binding site. G_{Cl}, G_{cation}, and G_{NMDA} are the inhibitory, excitatory, and NMDA conductances in units of nanosiemens (nS). V (mV) is the corrected holding potential. Since K_{Mg} and V_{δ} determine the shape of the nonlinear NMDA I–V relationship, it is critical to determine their values for the ON and OFF parasol cells. We used two approaches to isolate the synaptic NMDA I–V relationship (further illustrated graphically in Figs. 9 and 10 of the Results section).

The first approach isolated the NMDA response for both ON and OFF parasol cells (see Fig. 9) by subtracting the stimulus-evoked chloride and cation synaptic currents (5 Hz, 100% contrast, 1.1×10^5 photons/s/μm^2) measured while the NMDA receptors were blocked by D-AP5 from the total currents measured before drug application. We generated a mean NMDA I–V relationship for each cell by subtracting the drug I–V values from the control I–V values and fitting eqn. (1) at each time point that exhibited a large response amplitude. G_{cation} and G_{Cl} were set to zero. The resulting K_{Mg} and V_{δ} values were then averaged across time points. The average parameters were then inserted back into eqn. (1) which was evaluated from $V = -120$ to 40 mV to generate an average calculated NMDA I–V relationship for that cell. G_{NMDA} was set to the mean value across cells in order to normalize conductance amplitude. This calculated *I–V* curve represents the shape but not the absolute amplitude of the NMDA *I–V* for the cell. Finally, the calculated *I–V* curves for all ON and OFF cells were averaged and the average curve was itself fit with eqn. (1). For these data, K_{Mg} = 3.5 mM; V_δ = 22 mV (see Fig. 9).

The second approach isolated the NMDA response in four ON parasol cells by blocking the nonNMDA currents. We measured the isolated NMDA-mediated *I–V* relationship after the combined block of $GABA_A$, $GABA_C$, glycine, and AMPA/KA receptors (see Fig. 10 for details of the experimental conditions). As for the difference method, mean NMDA *I–V* parameters K_{Mg} and V_δ were calculated for each cell by fitting the *I–V* data at the high amplitude time points (gray shading in Fig. 10) with eqn. (1) and averaging the estimated parameters across time. The mean K_{Mg} and V_δ values for each cell, along with the mean NMDA conductance, G_{NMDA}, across cells were assigned to the parameters of the $I(V)$ equation which was evaluated from $V = -120$ to 40 mV. G_{cation} and G_{Cl} were again set to zero. The resulting calculated NMDA *I–V* curves for each of the four cells were plotted in Fig. 10C (middle panel). These calculated *I–V* curves represent the shape but not the absolute amplitude of the NMDA *I–V* curve for the cell. The solid red curve in Fig. 10 is the mean calculated NMDA *I–V* curve of all four cells. It was calculated as just described for the individual cells except that K_{Mg} and V_δ were the means of the values of the four cells. Using this approach $K_{Mg} = 3.3 \pm 0.6$ mM (mean ± S.D.) and $V_\delta = 19.5 \pm 1.7$ mV (mean ± S.D.). Finally, for the same cells, the proportion of conducting NMDA channels, $f(V)$, was plotted separately as a function of voltage (Fig. 10C, inset to middle panel). For these K_{Mg} and V_δ values, half maximal conductance occurs at −20 mV.

Both approaches gave essentially the same result for the shape of the NMDA-mediated *I–V* relationship. For subsequent analyses (Figs. 11 and 12), K_{Mg} and V_δ were set to 3.5 mM and 20 mV. We scaled the NMDA conductance magnitude to the chord conductance at −55 mV to better reflect the relative NMDA *versus* AMPA contribution at normal physiological voltage.

Light stimulation

All light stimuli were projected onto the retina *via* an optical system that delivered light *via* a camera port on the light microscope and utilized a 20× water immersion objective to focus a rectangular stimulus 700 × 1000 μm at the level of the photoreceptor outer segments. Two separate light sources shared the same optical relay. The first was a digital light projector (Vista-GraphX 2500, Christie Digital, Cypress, CA). Light from red, green, and blue primaries (dominant wavelengths of 636, 550, and 465 nm) were combined and with calibrated filtering provided quantal catch rates for the L and M cones (parasol cells receive summed input from L and M cones with little or no input from S cones) of ~2.5×10^5 photons/s/μm^2. These quantal catch rates are in the mid to high photopic range and we have previously shown that rods are in saturation at these light levels (Crook et al., 2009*a*). As previously discussed (Crook et al., 2011), given the uncertainties of the size of the cone aperture that strongly influence the efficiency of photoisomerization, we consider our estimates of quantal catch as very conservative. The digital light projector was used to project spatially discrete spots and annuli of varying diameters as well as extended grating stimuli that were sinusoidally modulated in contrast around a mean level (L), % Michelson contrast, where the contrast was defined as $(L_{\max} - L_{\min})/(L_{\max} + L_{\min}) \times 100$.

A second light-emitting diode (LED)-based stimulator (Pokorny et al., 2004; Crook et al., 2009*a*) was used to deliver temporally modulated “full-field” stimuli, that is, that lacked spatial structure and extended over the entire stimulus field. The LED-based stimulator had the advantage of reaching very high stimulus temporal frequencies of over 60 Hz with no loss of stimulus contrast and was used to characterize the high temporal frequency response of the parasol ganglion cells. Red, green, blue, and cyan primary LED channels (dominant wavelengths, respectively 561, 531, 430, and 491 nm) were combined and filtered to achieve quantal catch rates approximating $\sim 1.1 \times 10^5$ photons/s/μm^2 for the L and M cones. At each holding potential, the full field LED-based stimuli were repeated and the evoked synaptic currents were averaged. Stimulus repetition increased from 2 (50–100% contrast; 5–10 Hz) to 5 (6–25% contrast, 20–30 Hz) as contrast decreased or temporal frequency increased.

Contrast-response functions for the spike and peak conductances were fit with a Naka–Rushton saturation function: $Y = R_{\max} \times x/(C_{50} + x)$, where $R_{\max}$ is the maximal response in impulses per second, x is the Michelson contrast, and C_{50} is the semisaturation constant (the contrast at which the response amplitude is half the maximal response). Such curves are characterized by their percentage contrast gain, which is determined by using the fits to calculate $R_{\max}/C_{50}$. The goodness of fit was quantified using the standard error of the residuals, denoted $s_{\boldsymbol{e}}$.

Application of receptor antagonists

The following chemicals, all purchased from Sigma-Aldrich (St. Louis, MO), were added either alone or in combination to the Ames medium and applied to the entire retina *via* the superfusion: the glycine receptor antagonist strychnine (1 μM, S8753, Sigma), the $GABA_A$ receptor antagonist SR-95531 (GABAzine; 5 μM, S106, Sigma), the $GABA_C$ receptor antagonist (1,2,5,6-tetrahydropyridin-4-yl) methylphosphinic acid (TPMPA; 50 μM, T200, Sigma), the NMDA receptor antagonist, D-(−)2-amino-5-phosphonopetanoic acid (D-AP5; 50 μM, #0106, Tocris Bioscience, Minneapolis, MN), the AMPA receptor antagonist 2,3-dioxo-6-nitro-l,2,3,4-tetrahydrobenzo[*f*]quinoxaline-7-sulfonamide disodium salt (NBQX; 10 μM #1044, Tocris Bioscience) and the GLU_{K5} kainate receptor antagonist (*S*)-l-(2-amino-2-carboxyethyl)-3-(2-carboxy-thiophene-3-yl-methyl)-5-methylpyrimidine-2,4-dione (UBP 310, 10 μm #3621, Tocris Bioscience). Chemicals were maintained in separate oxygenated flasks and were delivered to the retinal superfusion chamber with a 6 channel valve controller (Warner Instruments, Hamden, CT, VC6) *via* a single manifold; due to the relatively large size of the incubation chamber needed to hold the primate retina wash-in and wash-out of the antagonist solution required ~2 min of superfusion.

Statistics

Throughout the Results, we summarize the data and record the mean ± standard error (s.e.) unless stated otherwise. The numbers of cells in each sample are recorded in the figures. To demonstrate the efficacy of our experiments, we utilize two-sample *t*-tests. The null hypothesis (H_0) is that the mean of the control population (μ_{control}) parameter is less than or equal to (greater than or equal to) the mean of the corresponding parameter in the experiment ($\mu_{experiment}$)-The alternative hypothesis (H_1) is that the control population parameter is greater than (less than) the experiment parameter. Almost all tests are one-tailed, as the mean results of a given experiment will either be significantly greater than or significantly less than the control mean. We utilize two-tailed tests to demonstrate that two independent sets of measurements have statistically similar means. We assume that the data belong to populations with unequal variances along the parameter of interest.

Results

Parasol cells display rectified synaptic excitation and crossover inhibition

Both ON- and OFF-center parasol cells are readily identifiable relative to other primate ganglion cell types by their very large cell body diameters and can therefore be reliably targeted under microscopic control *in vitro* (Fig. 1A). To begin to identify synaptic inputs that shape the spatial and temporal–contrast sensitivity of the parasol cell, it was convenient to start by measuring the temporal pattern of stimulus-evoked synaptic currents in response to a large uniform field, approximately 1 mm in diameter, encompassing the receptive field center and surround. Stimuli were contrast modulated sinusoidally around a mean photopic level (the maximum light level was ~1.1×10^5 photons/s/μm^2, see Materials and methods) at a relatively low temporal frequency (5 Hz) and high contrast (100%). Note that because the stimulus initiated at the mean level, the increase in contrast to the peak of the sine wave is only 50%, followed by 100% contrast modulations as the wave moves from peak to trough and back to peak. Finally, there is a second 50% contrast modulation as the sine wave moves through the final 90 deg from the trough back to the mean level. At this temporal frequency and these contrasts spike discharge and postsynaptic currents were easily resolvable over the time course of the stimulus modulation (Fig. 1B and 1C). Thus the OFF cell shows an excitatory OFF spike discharge to two, 100% contrast decrements (Fig. 1B, left), whereas the ON cell shows an excitatory ON spike discharge at three contrast increments, a 50% increment from the mean followed by a 100% increment and finally a second 50% increment from trough to mean level (Fig. 1B, right).

The timing of spike discharge and the modulation of the underlying membrane potential in response to this stimulus (Fig. 1B) illustrates that for both the ON and OFF cells, the membrane potential depolarized during the spiking phase and hyperpolarized during the nonspiking phase. By contrast, synaptic currents evoked by this stimulus were distinctly nonlinear, displaying clearly rectified current families dominated by excitation (reversal potential near 0 mV) during the spiking phase and crossover inhibition (reversal potential ~ −65 mV) during the nonspiking phase (Fig. 1C and 1D). Thus postsynaptic inhibition present during the spiking phase of the response was small relative to the large and evident crossover inhibition. The half-wave rectified nature of the synaptic excitation and inhibition is clearly shown in the plots of excitatory and inhibitory conductances over the time course of the stimulus (Fig. 1E). Thus for both ON and OFF parasol cell types, depolarization of the membrane potential arises from an increase in excitatory conductance, with little contribution from the withdrawal of synaptic inhibition (disinhibition). Conversely, hyperpolarization is produced by an increase in an inhibitory conductance with little contribution from the withdrawal of excitation (Fig. 1E).

Note that inspection of the *I–V* plots in Fig. 1 during the excitatory response phase shows clear nonlinearity at negative holding potentials from approximately −100 to −50 mV for both ON and OFF parasol cells. It was therefore necessary to use the currents recorded at the more positive holding potentials (see Materials and methods) to estimate a linear slope conductance with a reversal potential at 0 mV. Many studies recording from retinal ganglion cell types in both mammals and nonmammals (Mittman et al., 1990; Diamond & Copenhagen, 1993; Cohen et al., 1994; Cohen, 1998; Manookin et al., 2010; Venkataramani & Taylor, 2010; Buldyrev et al., 2012) have shown that this nonlinearity is due largely to the well established NMDA receptor-mediated contribution to glutamatergic synaptic excitation of ganglion cells. In the following sections, we use receptor antagonists to resolve the GABAergic *versus* glycinergic contribution to postsynaptic inhibition, and NMDA *versus* AMPA/kainate receptor contribution to synaptic excitation. We then attempt to further resolve the contribution of these circuit components to spatial, temporal, and contrast sensitivity.

Postsynaptic inhibition is largely glycinergic and crossover

It is evident that for both the ON and OFF cell examples shown in Fig. 1, crossover inhibition is very large compared to feedforward inhibition (inhibitory conductance in-phase with the depolarizing voltage response) at the highest (100%) stimulus contrast. Fig. 2A and 2B show the mean excitatory and inhibitory conductances in response to a 5-Hz stimulus modulated at 50% contrast for an OFF and an ON cell. The peak amplitude of the crossover inhibitory conductance was approximately 4–7 times greater than the feedforward inhibition (feedforward *vs*. crossover for OFF cells, 9 ± 4 *vs*. 61 ± 23 nS; and for ON cells, 8 ± 2 *vs*. 35 ± 7 nS). We defined the peak amplitude as the largest mean conductance value across the two stimulus cycles.

Previous studies recorded from a number of different ganglion cell types have shown that crossover inhibition arises from glycinergic amacrine cells (Murphy & Rieke, 2006; Molnar et al., 2009; Werblin, 2010) and in some instances, at least can contribute, *via* disinhibition, to the excitatory spiking phase of the ganglion cell response to a light step (Manookin et al., 2008; van Wyk et al., 2009). To determine if this is true for ON and/or OFF parasol cells, we bath-applied receptor antagonists and measured the relative contribution of GABAergic and glycinergic inputs to the inhibitory conductance (Fig. 2C and 2D). $\mathrm{GABA_A}$ and $\mathrm{GABA_C}$ receptor antagonists, GABAzine (5 μM), and TPMPA (50 μM), elicited small and variable changes (Fig. 2C and 2D; right-tailed *t*-test, H_0: $\mu_{\mathrm{control}} \leq \mu_{\mathrm{GABA}}$, H_1: $\mu_{\mathrm{control}} < \mu_{\mathrm{GABA}}$) on the amplitude of the peak crossover inhibitory conductance (control *vs*. GABA receptor block: OFF cells 61 ± 23 nS *vs*. 47 ± 18 nS, *t*-test $P > 0.33$ or ON cells 35 ± 7 nS *vs*. 37 ± 6 nS, *t*-test $P > 0.41$), the peak feedforward inhibitory conductance (control *vs*. GABA receptor block: OFF cells 9 ± 4 *vs*. 2 ± 8 nS, *t*-test $P > 0.06$ or ON cells 8 ± 2 *vs*. 10 ± 2 nS, *t*-test $P > 0.35$) or the peak excitatory conductance (control *vs*. GABA receptor block: OFF cells 41 ± 9 *vs*. 46 ± 7 nS, *t*-test $P > 0.35$ or ON cells 40 ± 5 *vs*. 47 ± 9, *t*-test $P > 0.25$). By contrast, addition of strychnine (1 μM) abolished all crossover inhibition and confirmed its glycinergic origin (Fig. 2E and 2F, left-tailed *t*-test, H_0: $\mu_{\text{control}} < \mu_{\text{glycine}}$, H_1: $\mu_{\text{control}} < \mu_{\text{glycine}}$ OFF cells $P < 0.02$ and ON cells $P \ll 0.01$). In addition, strychnine significantly (right-tailed *t*-test, H_0: $\mu_{\text{control}} \geq \mu_{\text{GABA and glycine}}$, H_1: $\mu_{\text{control}} < \mu_{\text{GABA and glycine}}$) evoked an −30% increase in the peak excitatory conductance relative to controls (Fig. 2E control *vs*. GABA plus glycine receptor block: OFF cells 41 ± 9 *vs*. 60 ± 5, *t*-test $P < 0.05$; Fig. 2F ON cells, 40 ± 5 *vs*. 58 ± 8 nS, *t*-test $P < 0.04$). In OFF parasol cells, crossover inhibition was also abolished by application of L-AP4, the mGLuR6 receptor agonist ($n = 6$, data not shown), confirming that the ON pathway drives crossover inhibition in the OFF pathway *via* a glycinergic amacrine cell as observed in previous studies of OFF alpha cells in mouse and guinea pig (Manookin et al., 2008; van Wyk et al., 2009) and OFF X cells in rabbit retina (Buldyrev et al., 2012; Buldyrev & Taylor, 2013).

Block of glycinergic crossover inhibition unmasks crossover excitation

For both ON and OFF parasol cells, attenuation of crossover inhibition unmasks the presence of a smaller excitatory postsynaptic current. Crossover inhibition thus appears to mask a distinct excitatory input that peaks in the opposing phase to that of the center (Figs. 2 and 3). This “crossover excitation” was larger in ON cells (peak 31 ± 7 nS, $n = 9$) than OFF cells (peak 11 ± 4 nS, $n = 8$). In ON cells, the large crossover excitation underlies depolarization of the membrane potential and spike discharge that appears during a contrast decrement after the block of glycinergic inhibition (Crook et al., 2008*b*). The unmasked OFF excitatory input is also preserved in ON parasol cells after the addition of L-AP4 to block ON-pathway transmission ($n = 14$; data not shown) confirming that this excitatory conductance originates in the OFF pathway.

In sum, the synaptic signature for both ON and OFF parasol cells is characterized by rectified excitation and crossover inhibition. Thus the modulation of the membrane potential and spike discharge to a sinusoidal stimulus is achieved by an increase in excitation during the spiking phase followed by an increase in inhibition during the nonspiking phase; the two rectified conductances appear to work synergistically to elicit a more linear modulation of the membrane potential (Fig. 1B). Crossover inhibition is glycinergic and is the dominant form of postsynaptic inhibition for both the ON and OFF cells. Feedforward GABAergic inhibition is present but at least in response to the stimuli used here, which is small compared to the glycinergic crossover inhibition.

The antagonistic surround is generated presynaptically without synaptic inhibition

Cone photoreceptors (Verweij et al., 2003; Packer et al., 2010) and cone bipolar cells (Dacey et al., 2000) in primates show a clear center–surround organization. Thus, the surround observed at the ganglion cell level would be expected to arise at least in part presynaptically. Previous work on the parasol as well as midget ganglion cell surrounds in primates found that attenuation of GABAergic and glycinergic transmission had only a small effect on surround strength and it was concluded that a nonGABAergic horizontal cell-mediated feedback mechanism (Verweij et al., 1996; Kamermans et al., 2001; Hirasawa & Kaneko, 2003; Fahrenfort et al., 2009) provided the major source of the surround (McMahon et al., 2004; Davenport et al., 2008; Crook et al., 2011). Our goal here was to use the voltage clamp to more directly test the hypothesis that presynaptic modulation of bipolar cell excitatory output provides the major origin of the parasol cell surround. Optimal spot and annular stimuli were determined before changing to the whole-cell recording configuration by recording spike responses in the loose patch configuration to a series of spots of increasing diameter and annuli of increasing inner diameter. Based on the peak spike discharge and the response phase, we determined respectively the spot diameter and annulus inner diameter that best isolated the center and surround.

Fig. 3 first illustrates the synaptic current families and associated conductances generated by center-spot and surround-annular stimuli and shows that for both ON and OFF parasol cells, both synaptic excitation and crossover inhibition as described in Figs. 1 and 2 are phase shifted ~180 deg by the surround engaging annular stimulus, consistent with the effect of this stimulus on the voltage response (Fig. 3A-3D, compare top traces). Thus for an ON cell, synaptic excitation shifts in phase from stimulus increment to decrement and crossover inhibition shifts from stimulus decrement to increment (Fig. 3C *vs*. Fig. 3D), and *vice versa* for the OFF cell (Fig. 3A *vs*. Fig. 3B). The block of all synaptic inhibition isolates the synaptic excitation and elicits the expected ON–OFF excitatory current to the spot stimulus (see Fig. 2; Fig. 3A and 3C bottom traces-inhibitory block) and this excitation is maintained, again with an ~180 phase shift during annular stimulation of the surround (Fig. 3B and 3D, bottom traces-inhibitory block). Thus, the voltage clamp data show directly that the surround response to an annulus is driven by strong modulation of glutamate release by the cone bipolar cells presynaptic to the parasol cell. Moreover, attenuation of all synaptic inhibition does not reduce the surround response to an annulus suggesting strongly that neither pre- nor postsynaptic inhibition contributes directly to the surround. However, the synaptic excitation evoked by spot, annular, and large diameter stimuli (see Fig. 2 above) shows an increase in peak conductance amplitude after attenuation of glycinergic synaptic inhibition, suggesting that glycinergic amacrine cells act presynaptically to suppress bipolar cell output (right-tailed *t*-test, H_0: $\mu_{\text{control}} \geq \mu_{\text{GABA and glycine}}$, H_1: $\mu_{\text{control}} < \mu_{\text{GABA and glycine}}$: OFF cells, spot: 69 ± 14 to 124 ± 53 nS, *t*-test $P > 0.18$; annulus, 31 ± 7–89 ± 14 nS, *t*-test $P \ll 0.01$; ON cells, spot: 62 ± 11–107 ± 20 nS, *t*-test $P > 0.05$; annulus: 80 ± 9–122 ± 25 nS, *t*-test $P > 0.09$).

In sum, the phase reversal of the spike discharge in response to spot *versus* annular stimuli shown in Fig. 3A–3D (top traces) is explained by an underlying phase reversal in the excitatory synaptic conductance. The surround therefore originates largely presynaptic to the ganglion cells consistent with the strong center–surround organization of primate cone bipolar cells. We also conclude that the preservation of the surround response evoked by an annulus after the combined block of GABA and glycine receptors is consistent with a horizontal cell negative feedback mechanism that does not require synaptic inhibition. Finally, the phase reversal of both the excitatory and crossover inhibitory conductances also adds the additional detail that the direct inhibitory input that generates crossover inhibition must also have a surround that originates presynaptically.

Synaptic excitation mediates nonlinear spatial summation

Parasol cells show the nonlinearity of spatial summation characteristic of the alpha-Y cells of other mammalian species (Enroth-Cugell & Robson, 1966; Demb et al., 1999; Crook et al., 2008*b*). A succinct picture of the spatial nonlinearity is captured in what has been called the Y-cell signature (Spitzer & Hochstein, 1985; Shapley & Perry, 1986; Crook et al., 2008*b*). The Y-cell signature appears in a plot of the spatial frequency tuning of the linear first harmonic (F1) response at the temporal frequency of a drifting grating compared to a plot of the second harmonic (F2) response to counterphase modulation of a stationary grating (Fig. 4A). These two plots illustrate the higher spatial resolution for the F2 relative to the F1 response components. Thus, the F2 response (Fig. 4B, right) originates from nonlinear summation of receptive field subunits that are smaller in diameter, and thus displays a higher spatial resolution, than the center mechanism (Hochstein & Shapley, 1976). A key feature of the F2 nonlinear spatial summation is that it is independent of stimulus phase or position (Fig. 4A, right inset plot), whereas the linear F1 spatial summation is sensitive to stimulus location (Fig. 4A, left inset plot). Evidence has been presented from previous experiments in guinea pig, mouse, and for parasol cells in primates that the subunits correspond to an array of transient partially rectifying bipolar cell inputs to the receptive field (Demb et al., 2001; Crook et al., 2008*b*; Schwartz et al., 2012). However, models have also been proposed that require summation utilizing synaptic inhibition *via* amacrine cells (Victor & Shapley, 1979; Frishman & Linsenmeier, 1982). It has also been proposed more recently that crossover inhibition could either play a critical role in compensating for the rectified output of bipolar cells to reduce or eliminate the Y-cell nonlinearity (Molnar et al., 2009; Werblin, 2010) or contribute to shaping the time course of the F2 response (Cafaro & Rieke, 2013). Here, we use high spatial frequency, contrast-reversing gratings to isolate the F2 response component and directly measure the evoked synaptic currents that underlie the Y-cell F2 response in parasol cells.

Thus to isolate the optimal F2 response, we first recorded extracellularly and mapped the F2 spatial tuning curve. The spatial frequency that elicited the peak, spatial phase insensitive F2 response was then used to measure evoked synaptic currents in the same cell after establishing a whole cell recording. In response to stimulus modulation at a spatial frequency at the peak of the F2 response (100% contrast; diameter = 1000 μm; 3.29 cycles/deg; Fig. 4A), the spike discharge and underlying membrane potential is modulated at twice the stimulus temporal frequency (Fig. 4B). In voltage clamp, the underlying stimulus-evoked synaptic currents show a corresponding frequency doubled modulation for both ON and OFF cell types (Fig. 4C). Resolution of the underlying conductances reveals that both synaptic excitation and crossover inhibition are modulated at twice the stimulus frequency; both conductances peak four times to two cycles of a sinusoid. To assess the phase and timing delays between the peak excitatory and inhibitory conductances, we calculated the difference between the closest peaks in time and report the average difference in milliseconds. For the ON cells, the peak excitatory and inhibitory conductances were nearly in-phase, but with the peak inhibitory conductance slightly leading excitation (Fig. 4D, right; 13 ± 3 ms). For the OFF cells, however, the peak excitatory conductance was instead clearly phase advanced relative to the peak inhibitory conductance (Fig. 4D, left; 33 ± 3 ms).

We showed previously that GABA receptor antagonists did not alter the spatial tuning of the F2 response elicited by contrast reversing grating stimuli (Crook et al., 2008*b*). Here we find that bath application of $GABA_A$ and $GABA_C$ receptor antagonists (GABAzine, 5 μM;

TPMPA, 50 μM) did not alter the temporal pattern of frequency doubled excitatory and inhibitory conductances (Fig. 4E). The timing differences between the peak excitatory and inhibitory conductances did not change significantly for OFF or ON cells (right-tailed *t*-test, H_0: $\mu_{\text{control}} \geq \mu_{\text{GABA}}$, H_1: $\mu_{\text{control}} < \mu_{\text{GABA}}$; OFF cells $P > 0.20$ and ON cells $P > 0.12$). However, the amplitude of the peak excitatory and inhibitory conductances was asymmetrically affected for OFF *versus* ON cells. For the OFF cells, the peak excitatory conductance increased significantly from 17 ± 2 to 28 ± 2 nS (*t*-test $P \ll 0.01$) but not for the peak inhibitory input (20 ± 3 *vs*. 17 ± 1 nS, *t*-test $P > 0.18$). There was no significant change for the ON parasol cells peak inhibitory (16 ± 2 *vs*. 18 ± 1 nS, *t*-test $P > 0.19$) or peak excitatory conductance (22 ± 3 *vs*. 25 ± 4 nS, *t*-test $P > 0.25$). These results suggest a presynaptic effect of GABAergic synaptic inhibition acting on the OFF pathway at high spatial frequencies not previously observed in response to a large diameter stimulus (Fig. 2).

The large frequency doubled inhibitory conductance corresponds to the dominant glycinergic crossover inhibition. Addition of strychnine (1 μM) abolished the inhibitory conductance completely; the timing of the peak excitatory conductances again did not change significantly for OFF or ON cells (right-tailed *t*-test, H_0: $\mu_{\text{control}} \geq \mu_{\text{GABA and glycine}}$, H_1: $\mu_{\text{control}} < \mu_{\text{GABA and glycine}}$; OFF cells $P > 0.38$ and ON cells $P > 0.32$). However, the frequency-doubled excitatory conductance showed a large and significant increase in amplitude for the ON cells but not the OFF cells (Fig. 4F; OFF cells: 28 ± 2 to 25 ± 2 nS, *t*-test $P > 22$; and ON cells: 25 ± 4 to 48 ± 3 nS, *t*-test $P \ll 0.01$).

This result is consistent with previous measurements of a preserved and elevated F2 spike discharge rate after the block of synaptic inhibition (Crook et al., 2008*b*). We conclude, first, that consistent with previous indirect results, the frequency doubled excitation is preserved, indeed increased, after elimination of all synaptic inhibition demonstrating clearly that summation of the excitatory cone bipolar inputs provide the origin of the Y-cell F2 response in both ON and OFF parasol cells. Second, since both the excitatory and glycinergic inhibitory conductances show the F2 response, it is possible, though not proven, that the same bipolar cells that provide the direct ON and OFF input to the parasol cells also provide the synaptic drive to the glycinergic amacrine cells that in turn mediate postsynaptic crossover inhibition. Third, the timing of the excitatory and inhibitory conductances varies for ON *versus* OFF cells to high spatial frequency contrast-reversing gratings. For the ON cells, excitation slightly lags inhibition (~10 ms), but for the OFF cells, excitation significantly leads (~30 ms) inhibition. Finally, the network effects of blocking GABAergic and glycinergic inhibition differ. For OFF cells, GABAergic block elicits an increase in amplitude of the F2 excitation, whereas for ON cells, attenuation of glycinergic inhibition elicits a large increase in the F2 excitatory conductance. These results suggest that for ON cells, small field glycinergic amacrines act presynaptically to suppress bipolar cell glutamate release under these stimulus conditions. However for OFF cells, it appears that GABAergic transmission serves such a role.

Crossover inhibition does not contribute to contrast gain in parasol cells

In OFF alpha-Y cells of mouse and guinea pig, withdrawal of glycinergic crossover inhibition (disinhibition) during the OFF phase of a light stimulus drives depolarization and spike discharge (Murphy & Rieke, 2006; Manookin et al., 2008; van Wyk et al., 2009), and evidence has been presented that the contribution from disinhibition increases near response threshold when stimulus contrast is low (Manookin et al., 2008). Both ON- and OFF-center parasol cells show clear glycinergic crossover inhibition; however, this inhibition is rectified with the result that there is little or no withdrawal of inhibition during the depolarizing spiking phase of the light response. Thus, the data presented so far (Figs. 1–4) would suggest that, at least at high contrasts, crossover inhibition makes no contribution *via* disinhibition to the light-evoked response in either ON or OFF parasol cells. A similar pattern of rectified crossover inhibition, distinct from that of OFF-alpha cells, has been recently observed in OFF-center brisk sustained ganglion cells of rabbit retina (Buldyrev et al., 2012).

To determine whether crossover inhibition contributes to contrast sensitivity in parasol cells, especially near response threshold, we first measured contrast sensitivity in the spike discharge after the block of synaptic inhibition. We measured contrast response functions modulated at both 4 and 30 Hz. Consistent with the expectation from the rectified nature of the crossover inhibition in parasol cells as well as the increase in the amplitude of the excitatory conductance after blockade of glycinergic transmission (Fig. 2E and 2F), spike discharge rates were elevated at all contrasts, at 4 and 30 Hz, for OFF (4 Hz, 58 ± 17% and 30 Hz, 59 ± 41%) and ON cells (4 Hz, 39 ± 66% and 30 Hz, 23 ± 21%) but more so for the OFF cells and especially at the highest contrasts (Figs. 5A and 6A). The block of synaptic inhibition increased the spike rates significantly (right-tailed *t*-test, H_0: $\mu_{\text{control}} > \mu_{\text{GABA and glycine}}$, H_1: $\mu_{\text{control}} < \mu_{\text{GABA and glycine}}$) for the OFF cells at all contrasts greater than 25% (*t*-test 4Hz $P \ll 0.01$ and 30 Hz $P \ll 0.01$). Correspondingly, contrast gain (taken as $R_{\max}/C_{50}$; see Materials and methods) also increased relative to control at both low and high temporal stimulus frequencies in OFF and ON parasol cells (Figs. 5A and 6A; control *vs*. inhibitory block: OFF cells: 4 Hz, 2.7 ± 0.4 *vs*. 4.7 ± 1.2, *t*-test $P > 0.09$ and 30 Hz, 3.3 ± 0.4 *vs*. 4.6 ± 0.7, *t*-test $P > 0.07$; ON cells: 4 Hz, 2.7 ± 0.26 *vs*. 2.9 ± 0.5, *t*-test $P > 0.35$ and 30 Hz, 4.0 ± 0.3 *vs*. 5.8 ± 1.0, *t*-test $P > 0.09$).

Direct measurement of ON- and OFF-cell synaptic conductances across stimulus contrasts from 6 to 50% revealed an unexpected result. The inhibitory conductance declined relative to the excitatory conductance as contrast was reduced for both ON and OFF types (Figs. 5B and 6B). Thus, at higher contrasts (50–100%) where spike rates increasingly saturate (Figs. 5A and 6A), the inhibitory conductance was equal to or greater than the excitatory conductance, but at 6% contrast, the conductance change was either largely or completely derived from a modulation of excitatory conductance with little or no contribution from crossover inhibition (Figs. 5D and 6D). In accordance with the results from measurements of spike discharge (Figs. 5A and 6A), elimination of all synaptic inhibition tended to increase contrast gains for OFF cells (control *vs*. inhibitory block 1.4 ± 0.3 *vs*. 2.5 ± 0.6, *t*-test $P > 0.09$) and ON cells (control *vs*. inhibitory block 1.4 ± 0.2 *vs*. 2.0 ± 0.4, *t*-test $P > 0.09$), presumably due to removal of both presynaptic and postsynaptic feedforward inhibition (Figs. 5C, 5E, 6C, and 6F). Note that mirroring the reduction in crossover inhibition with decreasing contrast, a similar loss of crossover excitation (unmasked by the block of inhibition; Figs. 5C and 6C) occurs at reduced stimulus contrasts (Fig. 6E). We conclude that, though a rectified crossover inhibition is prominent in both ON and OFF parasol cells, it is driven largely at contrasts above the linear response range (above 15% contrast) and thus plays no functional role *via* disinhibition, especially near response threshold.

Crossover inhibition is not essential for high temporal sensitivity

Parasol cells show high temporal sensitivity with peak responsivity at frequencies as high as 30–40 Hz for cells in the retinal periphery, and it has been suggested that synaptic inhibition may be critical for this property (Solomon et al., 2002), but the contribution of synaptic inhibition to temporal sensitivity has not been directly characterized. We first measured the effect of GABA and glycine receptor antagonists on the temporal frequency response of the spike discharge (50% contrast modulation; 1mm diameter field). For a sample of 29 cells in the near retinal periphery, the corner frequency was 35–40 Hz, consistent with measurements made previously in the intact anesthetized monkey (Lee et al., 1990, 2007). We define the corner frequency as the temporal frequency at which the spike rate has declined to 0.7 of the peak on the high frequency falling limb of the tuning curve. For OFF parasol cells, the block of synaptic inhibition did not significantly change (right-tailed *t*-test, H_0: $\mu_{\text{control}} \geq \mu_{\text{GABA and glycine}}$, H_1: $\mu_{\text{control}} < \mu_{\text{GABA and glycine}}$) the temporal tuning, corner frequency, or spike rates (Fig. 7A; *t*-tests comparing spikes rates at each temporal frequency show that the *P* value was on average >0.30 ± 0.04). By contrast, for the ON parasol cells, the block of inhibition elicited, as anticipated from the results already shown for a 5-Hz stimulus in Fig. 2, a strong frequency doubled response at low temporal frequencies without a significant change in the corner frequency or average spike rate (Fig. 8A; *t*-tests comparing spikes rates at each temporal frequency show that the *P* value was on average >0.31 ± 0.07).

We then measured the synaptic currents evoked by the same stimulus at temporal frequencies of 5, 10, 20, and 30 Hz and also found differences between ON and OFF cells in the relative timing and amplitude of excitatory and inhibitory synaptic conductances (Figs. 7B-7E and 8B–8E). For the OFF parasol cells, crossover inhibition was diminished in amplitude (Fig. 7E) and showed an increased phase lag relative to excitation as temporal frequency increased (phase shift of ~120 deg from 5 to 30 Hz). Thus with increasing stimulus temporal frequency, inhibitory conductance drops in relative amplitude and shifts from near antiphase to near in-phase with excitatory conductance. For ON cells, by contrast, crossover inhibition was clearly maintained at high temporal frequencies (Fig. 8E), and the peak of the excitatory and inhibitory conductance also shifted to near in-phase (phase shift of ~150 deg from 5 to 30 Hz). Attenuation of GABAergic and glycinergic inhibitory conductances (Figs. 7B–7D and 8B–8D, right panels; Figs. 7F and 8F) tended to increase the peak excitatory conductance at all temporal frequencies for both ON and OFF. The increases were significant for the ON cells except at 30 Hz (amplitude of peak excitation before *vs*. after synaptic block: 5 Hz, 72 ± 10 *vs*. 103 ± 15 nS, *P* > 0.02; 10 Hz, 70 ± 13 *vs*. 97 ± 10 nS, *P* > 0.07; 20 Hz, 48 ± 9 *vs*. 72 ± 10 nS, *P* > 0.03; and 30 Hz, 29 ± 7 *vs*. 34 ± 12 nS, *P* > 0.36) but not for the OFF cells (amplitude of peak excitation before *vs*. after synaptic block: 5 Hz, 52 ± 12 *vs*. 74 ± 17 nS, *P* > 0.35; 10 Hz, 72 ± 16 *vs*. 85 ± 14 nS, *P* > 0.27; 20 Hz, 44 ± 7 *vs*. 53 ± 7 nS, *P* > 0.17; and 30 Hz, 38 ± 14 *vs*. 29 ± 5 nS, *P* > 0.29).

The timing of the peak excitatory conductances changed differently for the ON *versus* the OFF cells. For the OFF cells, there was no significant change in timing after the block of synaptic inhibition (time of peak excitation before *vs*. after synaptic block: 5 Hz, 251 ± 7 *vs*. 264 ± 7 ms, $P > 0.11$; 10 Hz, 197 ± 2 *vs*. 200 ± 3 ms, $P > 0.25$; 20 Hz, 169 ± 2 *vs*. 170 ± 2 ms, $P > 0.35$; and 30 Hz, 106 ± 2 *vs*. 107 ± 2 ms, $P > 0.40$). However for the ON cells, changes in the timing of the peak excitatory response to 5 and 10 Hz were small but significant (time of peak excitation before *vs*. after synaptic block: 5 Hz, 338 ± 3 *vs*. 347 ± 5 ms, $P > 0.06$; 10 Hz, 242 ± 4 *vs*. 256 ± 2 ms, $P \ll 0.01$; 20 Hz, 201 ± 2 *vs*. 204 ± 1 ms, $P > 0.15$; and 30 Hz, 93 ± 1 *vs*. 93 ± 1 ms, $P > 0.45$).

In sum, attenuation of synaptic inhibition produced no significant change in the spike rates across the temporal frequency response of both ON and OFF parasol cells. Similarly, the temporal response of the excitatory synaptic conductance shows a small increase in amplitude after the block of synaptic inhibition. ON and OFF cells differ in the temporal sensitivity of synaptic inhibition, with OFF cells showing greatly diminished inhibition relative to excitation at higher temporal frequencies, but a major role of this difference in ON *versus* OFF cell temporal tuning seems unlikely since the overall temporal frequency response of both ON and OFF cells is well preserved after the block of synaptic inhibition.

Characterization of NMDA receptor-mediated excitatory synaptic input to parasol cells

It is well established that both nonNMDA and NMDA receptors contribute to the light-evoked spike discharge of retinal ganglion cells (Boos et al., 1990; Massey & Miller, 1990; Mittman et al., 1990; Diamond & Copenhagen, 1993; Manookin et al., 2010; Venkataramani & Taylor, 2010; Buldyrev et al., 2012); indeed in the first study of the effects of glutamate receptor agonists and antagonists on primate ganglion cell physiology, an NMDA receptor contribution was clearly observed (Cohen & Miller, 1994), and it was concluded that NMDA receptor-mediated synaptic excitation made a small contribution to both the resting and light-evoked spike discharge of a variety of primate ganglion cell types.

More recently, it has been suggested that the presence and/or contribution of NMDA receptors may vary quite dramatically across ganglion cell types, with some types lacking, or largely lacking, NMDA receptors and other types showing an unexpectedly large NMDA conductance equal to, or in excess of, that mediated by the typically dominant AMPA/kainate receptors (Manookin et al., 2010; Buldyrev et al., 2012; Buldyrev & Taylor, 2013). Finally, there is evidence for variation in NMDA receptor subunit composition across cell types and that at least for some mammalian ganglion cell types, the NMDA receptor voltage-dependent conductance may be significantly higher at the resting membrane potential (Manookin et al., 2010; Venkataramani & Taylor, 2010; Buldyrev et al., 2012) than had been previously found from work in nonmammalian retina (Mittman et al., 1990) and assumed in modeling studies (Velte et al., 1997). Our initial goal therefore was to further evaluate the nonlinearities in the I–V relationship for excitatory conductance in ON and OFF parasol cells and to determine the overall contribution of NMDA receptors. A second goal was to isolate the NMDA current and model the voltage dependence of the NMDA-mediated conductance and use that relationship to resolve the NMDA contribution to temporal–contrast sensitivity in parasol cells.

For the great majority of ON and OFF parasol cells, the postsynaptic excitatory currents evoked by relatively high contrast modulation at low temporal frequencies (5 Hz; 50–100% contrast; Fig. 1) show a nonlinear *I* –*V* relationship at negative holding potentials, indicative of an NMDA receptor contribution (Fig. 9A and 9B). Application of D-AP5 (50 μM) results in a more linear *I*–*V* seen clearly in both the raw currents (magnified insets; Fig. 9A and 9B) and the *I*–*V* plotted at the peak of the excitatory phase (Fig. 9A and 9B, lower plots; OFF cell left, ON cell right). To provide an estimate of the NMDA receptor-mediated *I*–*V* relationship, we subtracted the control *I*–*V* from the *I*–*V* measured during D-AP5 application. The resulting *I*–*V* showed the characteristic negative slope conductance of an NMDA-mediated postsynaptic current and was fit using an equation that accounts for magnesium and voltage dependence of NMDA receptor gating (Ascher & Nowak, 1988; Manookin et al., 2010; Buldyrev et al., 2012) (see Materials and methods, eqn. 1) and describes the conductance–voltage relationship (Fig. 9C, OFF cell left plot; ON cell right plot). Data were similar for ON and OFF cells and were combined to arrive at a mean NMDA-mediated *I*–*V* (Fig. 9C, middle plot, $n = 9$, 6 OFF and 3 ON cells). This *I*–*V* gave an NMDA current with a half maximal conductance at −20 mV ($K_{Mg} = 3.5$; $V_{\delta} = 22$ mV, see Materials and methods for details).

In the above measurements, synaptic inhibition was not blocked and the NMDA-mediated postsynaptic current was not directly measured. Therefore to further establish the validity of this measurement, we attempted to more directly isolate the NMDA receptor-mediated synaptic current in ON parasol cells by blocking nonNMDA ionotropic receptors with a combination of AMPA/kainate receptors (NBQX; 10 μM) and kainate receptor antagonists (UPB 310, 10 μM) as well as $GABA_A$ (GABAzine, 5 μM), $GABA_C$ (TPMPA, 50 μM), and glycine receptor (strychnine, 1 μM) antagonists. The rationale was that these antagonists would isolate glutamatergic transmission from cone photoreceptors to ON bipolar cells *via* the mGluR6 receptor and from ON-bipolar cells to ganglion cell NMDA receptors. Application of these “NMDA-isolating” antagonists in ON parasol cells results in a small but very reproducible light-evoked current (Fig. 10A and 10B) whose *I*–*V* relationship is well fit by parameters (Fig. 10C, middle plot; $K_{Mg} = 3.3 \pm 0.6$ mM; $V_{\delta} = 19.5 \pm 1.7$ mV; half maximal conductance = −19.5 mV) nearly identical to those used to fit the “difference” *I*–*V* derived from subtracting control from D-AP5 conditions in Fig. 9. This current is completely abolished by addition of D-AP5 (Fig. 10B) to the bath, and we conclude that this *I*–*V* relationship provides a good estimate of the NMDA-mediated conductance in parasol cells.

With this fit to the data, the NMDA conductance is half maximal at approximately −20 mV (Fig. 10C, inset). This estimate appears consistent with previous measures of the NMDA conductance– voltage relationship for NMDA receptors with high Mg^{2+} affinity comprised of GluN2A and/or GluN2B subunits (Monyer et al., 1994; Kumar & Huguenard, 2003; Paoletti, 2011; Wyllie et al., in press) but differs from recent estimates for other mammalian ganglion cell types that suggest a greater NMDA-mediated conductance in the physiological range (Manookin et al., 2010; Venkataramani & Taylor, 2010; Buldyrev et al., 2012). We used these fit parameters for the NMDA conductance to resolve the relative NMDA (G_{NMDA}) *versus* nonNMDA receptor ($G_{AMPA/Ka}$) contribution to the total excitatory conductance as described in Materials and methods (Venkataramani & Taylor, 2010). We scaled G_{NMDA} as the chord conductance at −55 mV (~20% of maximal conductance) to better estimate the NMDA receptor contribution to total conductance during depolarization from the resting membrane potential. Fig. 10D illustrates the use of this model (see Materials and methods for details) to resolve the NMDA *versus* AMPA/Ka receptor contributions to the total conductance for the control and pharmacologically isolated NMDA light-evoked excitatory currents across the time window bracketed by dotted lines in Fig. 10A and 10B (top traces, control; middle traces, NMDA). The windowed control and NMDA-mediated currents are excised and reproduced in Fig. 10D and 10E. The *I–V* plots below the current families illustrate the model fit (black line through data points) for a single time point near the peak of the evoked currents (gray vertical line). The model provides a good fit to the nonlinear *I–V* and illustrates the linear inhibitory (G_{in}, red line), linear excitatory ($G_{\mathrm{AMPA/Ka}}$, blue line), and nonlinear NMDA (G_{NMDA}, green line; dotted green line, NMDA chord conductance at −55 mV; $G_{\mathrm{NMDA\text{-}55}}$) derived from this fit to the data. For the ON cell examples in Fig. 10A and 10B, the NMDA conductance at peak is 18 and 30% of the total excitatory conductance, respectively, and is slightly delayed relative to the peak of the AMPA/Ka conductance (15 and 12 ms, respectively).

NMDA receptors are not critical for contrast gain in parasol cells

Recent findings from experiments in guinea pig (Manookin et al., 2010) and rabbit retina (Buldyrev et al., 2012) suggest that for certain ganglion cell types, including OFF alpha-Y cells, an NMDA receptor-mediated conductance contributes strongly to light-evoked spike discharge near contrast threshold. Although a contribution to the light-evoked spike discharge and even the resting discharge of ganglion cells has long been recognized (Boos et al., 1990; Massey & Miller, 1990; Cohen & Miller, 1994), these new findings are unexpected since the earlier view was that most NMDA receptors, because of the high Mg^{2+} affinity of the receptor, would not contribute critically to the synaptic conductance until a neuron was sufficiently depolarized to significantly relieve the Mg^{2+} block of the NMDA receptor channel (Diamond & Copenhagen, 1993).

To address this question for parasol cells, we first quantified the effect of D-AP5 bath application (50 μM) to determine the contribution of NMDA receptors to the contrast sensitivity of parasol cells recorded extracellularly. For both ON and OFF cells, sensitivity was largely maintained over the linear portion of the contrast response (3–15%) in the presence of D-AP5. This was reflected in the contrast gain values that also did not change significantly (Fig. 10A and 10B; control *vs*. D-AP5: OFF cells 3.8 ± 1.1 *vs*. 4.7 ± 1.1, *t*-test $P > 0.25$; and ON cells: 2.8 ± 0.5 *vs*. 2.1 ± 0.4, *t*-test $P > 0.16$). However, D-AP5 bath application did alter spike discharge rates for both cell types (left-tailed *t*-test, H_0: $\mu_{\mathrm{control}} - \mu_{\mathrm{AP5}}$, H_1: $\mu_{\mathrm{control}} > \mu_{\mathrm{AP5}}$), but that of D-AP5 was greater in the ON cells (Fig. 10A and 10B, inset plots). For the ON cells, spike discharge was reduced to ~0.65 of control values at the higher stimulus contrasts, (50–100% contrast: mean $P \ll 0.03$) and this increased at the lowest contrast to ~0.47 of control (6% contrast: $P > 0.10$). In the OFF cells, the reduction was only ~0.85 of control at the highest contrast (50–100% contrast: the average $P > 0.13$), and at the lowest stimulus contrast, D-AP5 actually tended to paradoxically increase spike discharge (~1.5) relative to control (6% contrast: $P > 0.19$). One difficulty in interpreting these results is that bath applied D-AP5 can have unknown effects on amacrine cell transmission in the inner retina in addition to a direct postsynaptic effect on ganglion cells. It is thus possible that differences in the effects of D-AP5 on ON *versus* OFF parasol cells, particularly the unexpected response increase in the OFF pathway at low stimulus contrasts, could be the result of D-AP5 acting presynaptically on amacrine cell circuitry.

The NMDA receptor contribution to the ON and OFF parasol cell contrast response was further explored using the voltage clamp, with and without the block of GABAergic and glycinergic transmission, by measuring the synaptic currents evoked at 6, 12, 25, 50, and 100% contrast modulation and resolving $G_{\text{AMPA/Ka}}$ and $G_{\text{NMDA-55}}$ using the parameters given in Fig. 10 to describe the voltage-dependent NMDA conductance (Fig. 11C and 11D). The two $G_{\text{NMDA-55}}$ and two $G_{\text{AMPA/Ka}}$ contributions calculated at each contrast for each condition (control *vs*. synaptic inhibition block) did not differ significantly regardless of whether we looked at control (12C–F, circles) *versus* synaptic inhibition block data (12C–F, diamonds) (two-tailed *t*-test, H_0: $\mu_{\text{control}} = \mu_{\text{GABA and glycine}}$, H_1: $\mu_{\text{control}} \neq \mu_{\text{GABA and glycine}}$; the mean *P* value for the peak conductance for OFF cells: AMPA > 0.61 ± 0.08 and NMDA > 0.34 ± 0.07; and for ON cells: AMPA > 0.22 ± 0.06 and NMDA > 0.54 ± 0.13).

We found that the contrast gain typical of the spike discharge (Fig. 11A and 11B) is mirrored by a large increase in $G_{\text{AMPA/Ka}}$ with increasing stimulus contrast (control and inhibition blocked contrast gain values: Fig. 11E, OFF cells 1.3 ± 0.7 and 1.6 ± 0.9; Fig. 11F, ON cells 0.7 ± 0.1 and 1.2 ± 0.2). By contrast, the smaller $G_{\text{NMDA-55}}$ shows poor contrast gain with little change in amplitude from 6 to 100% contrast (control and inhibition blocked contrast gain values: Fig. 11E, OFF cells 0.5 ± 0.2 and 0.2 ± 0.0; Fig. 11F, ON cells 0.2 ± 0.0 and 0.3 ± 0.1). The consequence of the disparate $G_{\text{AMPA/Ka}}$ *versus* $G_{\text{NMDA-55}}$ contrast gains is that $G_{\text{NMDA-55}}$ makes a fractionally larger contribution (~25–40%) at the lowest contrast, decreasing to ~15% at higher contrasts (Fig. 11G and 11H). The larger NMDA contribution at the lowest contrast appears to be mirrored in the larger reduction that is spike discharge for the ON cells after bath application of D-AP5 (Fig. 11B). However, for the OFF cells D-AP5 actually increased spike discharge rates from control values indicating a likely presynaptic effect of D-AP5 present in OFF but not in ON cells. Again the percent of $G_{\text{NMDA-55}}$ was not significantly different for control *versus* synaptic inhibitory block data (two-tailed *t*-test, H_0: $\mu_{\text{control}} = \mu_{\text{GABA and glycine}}$, H_1: $\mu_{\text{control}} \neq \mu_{\text{GABA and glycine}}$, on average, the *P* value was >0.50 ± 0.13 for OFF cells and >0.68 ± 0.07 for ON cells).

Effect of stimulus temporal frequency on NMDA conductance

The results shown in Figs. 9–11 characterized $G_{\text{NMDA-55}}$ at a stimulus temporal frequency of 5 Hz. However, as shown in Figs. 7 and 8, parasol cells show peak spike discharge in response to temporal frequencies between 10 and 40 Hz. It is well established that the light-evoked NMDA-receptor-mediated response has a slower time to peak and longer decay time than nonNMDA glutamate receptors (Mittman et al., 1990). We thus wanted to make an initial qualitative assessment of the time course and amplitude of NMDA receptor-mediated conductance with variation in stimulus temporal frequency in parasol ganglion cells (Fig. 12A and 12B). We measured $G_{\text{NMDA-55}}$ and $G_{\text{AMPA/Ka}}$ with (diamonds) and without inhibition blocked (circles) as in Fig. 11 in response to 10, 20, and 30 Hz stimulus modulations. The two $G_{\text{NMDA-55}}$ and two $G_{\text{AMPA/Ka}}$ contributions calculated at each temporal frequency for both conditions, except for the two $G_{\text{AMPA/Ka}}$ at 5 Hz for the ON cells, did not differ significantly regardless of whether we looked at control (12C–F, circles) *versus* synaptic inhibition block data (12C–F, diamonds) (two-tailed *t*-test, H_0: $\mu_{\text{control}} = \mu_{\text{GABA and glycine}}$, H_1: $\mu_{\text{control}} \neq \mu_{\text{GABA and glycine}}$, on average, the *P* value for the peak AMPA conductances was >0.37 ± 0.04 and >0.36 ± 0.07 for NMDA for OFF cells and >0.46 ± 0.13 and >0.82 ± 0.01 for ON cells, respectively). We found that the peak and roll off in the temporal frequency response between 5 and 30 Hz characteristic of the spike discharge (Figs. 7A and 8A) was mirrored by a corresponding peak and roll off in the AMPA/Ka-mediated conductance from between 5 and 30 Hz temporal frequency (Fig. 12C and 12D). By contrast, between 5 and 30 Hz, the NMDA contribution changed little (Fig. 12C and 12D; OFF cell: 3.5 ± −0.6 nS; ON cell: 7.4 ± 1.5 nS). A consequence is that $G_{\text{NMDA-55}}$ makes a greater contribution to the total excitatory conductance at 30 Hz (Fig. 12E and 12F; 30 Hz: 20% for OFF and 28% for ON cells; 5 Hz: ~15% for both OFF and ON cells) due to the sharp roll off in the amplitude of the AMPA/Ka-mediated component.

Additionally, a clear and expected difference in response dynamics between the smaller G_{NMDA} and larger $G_{\text{AMPA/Ka}}$ was observed. On average, with and without inhibition blocked, across four temporal frequencies, the $G_{\text{NMDA-55}}$ peaked 7 ± 1 ms later than $G_{\text{AMPA/Ka}}$ for both ON and OFF cells. Thus, near the peak of $G_{\text{AMPA/Ka}}$ (Fig. 12A and 12B, bracketed insets) $G_{\text{NMDA5-5}}$ was either reduced or absent, and this was evident in the largely linear *I*–*V* relationship at early time points after stimulus onset even at the highest temporal frequency tested (Fig. 12A and 12B, inset *I*–*V* plots, 30 Hz).

In sum, an NMDA receptor-mediated conductance clearly contributes to the light-evoked postsynaptic excitatory current in both ON and OFF parasol cells. A similar contribution to both ON and OFF cell counterparts is quite distinct from that found for the alpha-Y cells in guinea pigs (Manookin et al., 2010) and the brisk-sustained-X cells in rabbits (Buldyrev et al., 2012; Buldyrev & Taylor, 2013) where only the OFF cells show evidence for an NMDA receptor-mediated conductance. NMDA receptors contribute about 20% to the total excitatory conductance across a broad range of contrasts and temporal frequencies, but the basic shape of the temporal–contrast sensitivity function appears to be mediated primarily by modulation amplitude of $G_{\text{AMPA/Ka}}$. The fraction of the total excitatory conductance contributed by $G_{\text{NMDA-55}}$ does increase at the lowest stimulus contrasts and highest temporal frequencies. However, contrast gain at low contrasts is not reduced by bath application of D-AP5 arguing against a critical role for the slower NMDA-mediated conductance in driving light-evoked discharge near response threshold in parasol cells.

Discussion

Glycinergic crossover inhibition present in ON and OFF parasol cells

Both ON- and OFF-center parasol cells show a distinctive mirror-image signature of excitatory and inhibitory conductances, in which largely rectified excitation and glycinergic crossover inhibition alternate during the depolarizing and hyperpolarizing phase of the voltage response to contrast increment and decrement (Fig. 1). The glycinergic inhibitory conductance was large at stimulus contrasts of 50–100% and similar in amplitude to the total excitatory conductance; by contrast, the GABAergic inhibition comprised only a small fraction of the total postsynaptic inhibitory conductance, a somewhat unexpected result, given the anatomical evidence that GABAergic and glycinergic receptors appear on parasol cell dendrites at relatively equal densities (Grünert & Ghosh, 1999; Grünert, 2000; Lin et al., 2000; Macri et al., 2000; Abbott et al., 2012). However, application of GABA receptor antagonists consistently produced only a very small positive shift in reversal potential consistent with a correspondingly small feedforward GABA-mediated inhibitory conductance. It seems unlikely that the relatively small GABAergic postsynaptic inhibition is stimulus dependent as similar stimuli produce greater feedforward inhibition in midget ganglion cells (Crook et al., 2011), and recently, in parallel with the present study, a similar dominance of glycinergic over GABAergic inhibition in ON parasol cells was reported using a 560-μm spot stimulus (Cafaro & Rieke, 2013).

What is the functional significance of crossover inhibition in parasol cells? Previous recordings from amacrine, bipolar, and ganglion cells in rabbit retina led to the conclusion that at least one major function of crossover inhibition is to provide circuitry that removes, or compensates for, the nonlinear distortion produced by rectified synaptic output of transient bipolar cells, and thus serves to produce a more linear signal transmission in ganglion cells (Molnar et al., 2009; Werblin, 2010, 2011). The fundamental dynamics of synaptic excitation and inhibition in parasol cells appears, at least qualitatively, to provide a near perfect example of this type of linearizing function, at least when high stimulus contrasts evoke large conductances. Excitatory and inhibitory conductances are strongly rectified, out of phase, and similar in amplitude, but the summation of these two conductances in response to a sinusoidal modulation in contrast produces a more linear modulation of the cell's membrane potential (Fig. 1). In addition, crossover inhibition in parasol cells appears to cancel excitation from an underlying excitatory crosstalk between ON and OFF pathways, which would produce additional response distortion. However, extreme rectification and the presence of both crossover inhibition and crossover excitation are most prominent at stimulus contrasts above 25%, where the spike discharge begins to saturate. At low stimulus contrasts, both crossover inhibition and crossover excitation diminish greatly, and the conductance is a relatively isolated synaptic excitation (Figs. 5 and 6). Thus, the linear contrast gain that characterizes the parasol cell from contrast threshold to about 15% contrast does not require crossover inhibition and indeed neither crossover inhibition nor spurious crossover excitation are present.

Crossover inhibition and the frequency-doubled response

The suggestion that crossover inhibition can compensate for response rectification led to an intriguing and testable hypothesis: the presence or absence of crossover inhibition would distinguish X- from Y-type ganglion cells, respectively (Werblin, 2010). This hypothesis proposes specifically that the presence of rectification in output of transient bipolar cells (Demb et al., 2001; Crook et al., 2008*b*) is preserved in the frequency doubled response of Y cells because compensatory crossover inhibition is lacking in the Y cell circuitry. Our results from parasol cells show that crossover inhibition is in fact the dominant form of postsynaptic inhibition in this type of Y cell and is clearly present in the frequency doubled (F2) conductances elicited by stimulation with contrast reversing gratings of high spatial frequency (Fig. 4). However, although glycinergic inhibition could reduce the amplitude of the F2 response at high stimulus contrasts (Crook et al., 2008*b*), it appears not to serve to cancel and thereby remove this response component (Fig. 4). Recently, evidence was presented that crossover inhibition could function like feedforward inhibition and arise after only a short delay in ON parasol cells to make the F2 response more transient and thereby contribute crucially to the parasol cell response to stimulus spatial structure (Cafaro & Rieke, 2013). In the present results, we also found that the relative timing of excitation and crossover inhibition was altered in the F2 response component but differed from that reported by Cafaro et al. For ON cells, inhibition peaked slightly before excitation, whereas Cafaro et al. reported the opposite result that inhibition followed excitation with a brief delay. We also found for the OFF parasol cells that crossover inhibition followed excitation, but after a relatively long delay (Fig. 4D–4E). These different results likely reflect differences in stimulus spatial configuration used to elicit an F2 response. In the Cafaro et al. study, the stimulus was presented at a very low spatial frequency (560 μm diameter spot) where the F2 response component would be at or near threshold and dependent on a stimulus spatial location that nulls the dominant F1 response. By contrast, in this study, we used stimuli of high spatial frequency (~ 10× of that in the Cafaro et al. study) beyond the resolution limit of the linear F1 response to elicit an isolated and maximal F2 response that was independent of stimulus spatial phase (Fig. 4A). Finally, we found that attenuation of synaptic inhibition affected the amplitude but not the timing of the excitatory frequency doubled conductance (Fig. 4E–4F). Thus, any hypotheses about the role that crossover inhibition might play in shaping the spatially nonlinear response will require measurements of the timing of excitation and crossover inhibition as a function of both stimulus location (spatial phase) and spatial frequency.

Crossover inhibition and the homology of parasol cells with alpha cells

The presence of crossover inhibition in parasol cells and alpha-Y cells of nonprimate mammals reinforces the suggestion that parasol cells are the primate homologue of the alpha-Y cell (Crook et al., 2013). However, the properties of crossover inhibition for parasol cells discussed above also appear to differ substantially from that recently described for mouse and guinea pig alpha cells (Manookin et al., 2008; van Wyk et al., 2009). First, crossover inhibition is present in OFF but not ON alpha cells. Second, crossover inhibition is tonically active in mouse and guinea pig OFF-alpha cells so that during light decrement, a reduction in inhibitory conductance contributes, in a “push–pull” manner, to driving excitation and the spike discharge of ganglion cells. In addition, evidence has been presented that this disinhibition has a higher contrast sensitivity than excitation so that near-contrast threshold disinhibition plays a significant role in generating depolarization and spike discharge (Manookin et al., 2008). In striking contrast, in both ON and OFF parasol cells, as discussed above, the inhibition is strongly rectified so that there is no measurable disinhibition at moderate and high stimulus contrasts. Moreover, at the lower contrasts, where contrast gain is linear, crossover inhibition is absent. Thus, the clear role of disinhibition in driving the light response, especially near threshold, of OFF-alpha cells in mouse and guinea pig appears to be entirely absent in parasol cells.

It has also been strongly argued that the parasol cells might be more comparable functionally to the achromatic X-cells of the cat's retina (Shapley & Perry, 1986; Kaplan et al., 1990) and provide the primary substrate for the achromatic channel of human vision (Lee, 2011; Cooper et al., 2012). In this context, it is worth noting that the crossover inhibition shown here for the ON and OFF parasol cells is also distinct from that measured recently for the ON and OFF brisk-sustained cells of rabbit retina (Buldyrev et al., 2012; Buldyrev & Taylor, 2013), considered the rabbit homologue of the cat X-cell (Zeck et al., 2005). For both the rabbit OFF brisk-sustained cell and the primate OFF parasol cells, glycinergic crossover inhibition is the dominant form of postsynaptic inhibition and is not tonically active and therefore does not drive depolarization *via* disinhibition (Buldyrev et al., 2012). However for the rabbit ON-brisk sustained cell, an equally large direct glycinergic input is, decidedly, *not* a crossover type of inhibition but appears in-phase with the ON-excitatory conductance (Buldyrev & Taylor, 2013). Finally, it is striking that primate midget ganglion cells, also invoked as a possible correlate of the brisk-sustained X cells, lack a significant postsynaptic crossover glycinergic input (Crook et al., 2011). The major differences in the functional properties of crossover inhibition among parasol cells and comparable cell types in other mammals suggest that either there are fundamental differences among homologous cell types across species or that these various cell classes represent fundamentally distinct cell types with independent evolutionary functional origins. Given the great diversity of mammalian ganglion cell types that remain to be characterized at the level of synaptic mechanism and functional role, it is currently impossible to distinguish between these alternatives.

Surround antagonism arises largely presynaptically and without synaptic inhibition

It has been shown previously, for both ON and OFF parasol cells, that attenuation of GABAergic or glycinergic synaptic inhibition had only a small effect on center–surround receptive field structure (McMahon et al., 2004). By contrast, other agents that appear to interfere with horizontal cell negative feedback to cone photoreceptors without attenuation of synaptic inhibition (Vigh & Witkovsky, 1999; Kamermans et al., 2001; Hirasawa & Kaneko, 2003; Fahrenfort et al., 2004; Fahrenfort et al., 2009) can abolish the surrounds of both parasol (McMahon et al., 2004; Davenport et al., 2008), midget (Crook et al., 2011), and small bistratified-blue-ON (Crook et al., 2009*a*) ganglion cell types in primate. These results were consistent with the hypothesis that surrounds at the bipolar and ganglion cell level arise by a mechanism that is independent of GABAergic or glycinergic synaptic inhibition and moreover that lateral feedforward synaptic inhibition mediated either by amacrine cells in the inner retina or by horizontal cell transmission to bipolar cell dendrites in the outer retina plays only a minor role in establishing the surrounds of parasol, midget, and blue-ON ganglion cells (Crook et al., 2013). In the present study, we used the voltage clamp to determine the extent to which synaptic inhibition contributed to the antagonistic surround, either pre- or postsynaptically. It was striking that for both ON and OFF parasol cells, center (small spot) and surround (annulus) isolating stimuli elicited a clear phase reversal in the temporal pattern of excitation and inhibition, which corresponded to the phase reversal in the modulation of the membrane potential and spike discharge (Fig. 3). Moreover, surround stimulation did not evoke any change or increase in direct postsynaptic inhibition. We conclude that the basic center–surround structure arises presynaptically and is transmitted to parasol cells by modulation of an excitatory bipolar input that possesses a strong center–surround organization. A similar phase reversal of the glycinergic crossover inhibition shows that the amacrine cells that provide this input must also have a center–surround organization that arises presynaptically. The simplest hypothesis is that the ON and OFF cone bipolar cells that directly excite the parasol cells also excite the amacrine cells that provide the crossover glycinergic inhibition. Consistent with this picture, attenuation of synaptic inhibition with GABA and glycine antagonists does not attenuate the excitatory conductances elicited by the surround-isolating annulus. However, the amplitude of the excitatory conductances for both spot and annular stimuli was increased significantly by the block of synaptic inhibition showing that these transmitters act presynaptically to suppress bipolar cell output.

The recent results from concentrically organized brisk sustained ON and OFF rabbit ganglion cell types suggest a basic qualitative similarity in the synaptic origin of the surround (Buldyrev & Taylor, 2013). For this class of rabbit ganglion cells, the surround was also presynaptic in origin with a large component that was preserved after the block of synaptic inhibition. However, for the brisk-sustained cells in rabbit, it was striking that presynaptic inhibition acting to suppress center-mediated excitation was much stronger than that found in any primate ganglion cell thus far. Indeed for both the ON and OFF brisk-sustained cells, stimuli of large diameter completely suppressed light-evoked spike discharge and correspondingly almost completely suppressed any light-evoked conductance change (Buldyrev & Taylor, 2013). In parasol cells, presynaptic inhibition is also present, but in response to stimuli of large diameter, spike discharge remains high and synaptic currents are correspondingly large (Fig. 1).

Another recent study characterizing inner *versus* outer retinal contributions to the surrounds of ganglion cells in the larval tiger salamander also found that a nonGABAergic horizontal cell-mediated feedback mechanism made the primary contribution to the surround (Ichinose & Lukasiewicz, 2005). However, it was also reported that at low but not high photopic levels, a GABAergic pathway acting presynaptically on bipolar cells contributes to the surround. Since the present results for parasol cells were conducted at relatively high photopic levels, it remains possible that exploration of cone signals in the mesopic range (Cao et al., 2010) may reveal additional surround mechanisms.

NMDA receptor-mediated conductances in parasol cells

One previous study utilizing an *in vitro* preparation of the primate retina identified an NMDA receptor-mediated contribution to ganglion cell light-evoked spike discharge (Cohen & Miller, 1994) like that observed in other mammalian (Boos et al., 1990; Massey & Miller, 1990) and nonmammalian retina (Diamond & Copenhagen, 1993). Here, we extend this early observation to establish that parasol ganglion cells show NMDA receptor-mediated postsynaptic currents with a magnitude and conductance–voltage relationship that is very similar for both ON and OFF cell types (Figs. 9 and 10) and indicate a high Mg^{2+} binding affinity (half maximal conductance approximately −20 mV). High Mg^{2+} binding affinity is associated with NMDA receptors in which the requisite GluN1 subunits combine with either GluN2A or GluN2B subunits (Monyer et al., 1994; Wyllie et al., in press). Immunostaining of NMDA subunits in the inner plexiform layer (IPL) of macaque monkey provides some anatomical support for this picture (Grünert et al., 2002). It was shown that GluN2A immunoreactive puncta were localized to synapses in both the OFF and ON portions of the IPL at 20–40 and 60–80% depth, respectively and therefore overlap with the dendritic stratification of ON and OFF parasol cells (Crook et al., 2008*a*). Moreover, in a New World primate, the marmoset, the GluN2A subunit was also specifically localized to the axon terminal of a diffuse cone bipolar type (DB3) that is presynaptic to the OFF parasol cell (Jacoby & Marshak, 2000). The GluN2A puncta were colocalized with about 50% of the GluN1 subunits and so account for a large fraction, but likely not all, of the NMDA receptors in the IPL (Grünert et al., 2002); GluN2B, GluN2C, and GluN2D subunits remain to be identified in macaque retina. Thus, what is currently known about the spatial distribution of NMDA receptor subunits in the macaque IPL together with the basic properties of the NMDA receptor-mediated conductance shown here for parasol cells suggests an NR1–NR2A subunit composition as the most likely for both ON and OFF parasol cells. Given the relatively large NMDA current that can be isolated from ON parasol cells, it should be possible to directly test this hypothesis in future experiments with more detailed study of the kinetics, voltage dependence, and pharmacology of the NMDA-mediated conductance as well as more detailed cell type-specific localization of receptor subunits.

Although much remains to be learned about the structure, function, and distribution of NMDA receptors in identified ganglion cell types in mammalian retina, it is striking that the emerging picture for parasol cells differs substantially from that described recently for both the alpha-Y cells in guinea pigs (Manookin et al., 2010) and brisk-sustained-X cells in rabbits (Buldyrev et al., 2012; Buldyrev & Taylor, 2013). First, both of these cell classes comprise ON- and OFF-center types like the parasol cells, but only the OFF cells showed measurable NMDA receptor-mediated postsynaptic currents. Moreover, evidence was presented in these studies that the NMDA channel showed a surprisingly low Mg^{2+} binding affinity and presumably a much higher NMDA conductance at physiological membrane voltages than would be expected for receptors that utilize GluN2A and/or GluN2B subunits (Paoletti, 2011; Wyllie et al., in press). Similarly, an extremely low Mg^{2+} binding affinity—half maximal conductance approximately −70 mV—was reported for a class of orientation-selective ganglion cells in the rabbit retina (Venkataramani & Taylor, 2010). Finally, as discussed above, we found no differences in the voltage dependence, kinetics, or amplitudes of the NMDA-mediated postsynaptic currents in ON *versus* OFF parasol cells, which might suggest that these distinct cell classes differ in either the complement or subunit composition of the NMDA receptor. This also differs from an emerging picture in mouse and rat retina whereby ON cells utilize GluN2B subunits localized extrasynaptically, and OFF cells utilize GluN2A subunits placed synaptically (Sagdullaev et al., 2006; Kalbaugh et al., 2009; Zhang & Diamond, 2009). Continued experiments designed to carefully isolate and characterize the NMDA contribution to various ganglion cell types are required to determine the degree to which these initial observations represent true functional variation across species and/or ganglion cell types.

We used the nonlinear *I–V* relationship of the pharmacologically isolated NMDA current in parasol cells to model the voltage dependence of the NMDA conductance and thereby estimate its contribution to the total stimulus-evoked conductance change (Manookin et al., 2010; Venkataramani & Taylor, 2010; Buldyrev & Taylor, 2013). In two previous studies using the same method, it was suggested that for the OFF alpha-Y cells of guinea pig (Manookin et al., 2010) and the OFF-brisk sustained-X cells of rabbit retina (Buldyrev & Taylor, 2013), the NMDA contribution comprised a larger fraction of the total excitatory conductance near response threshold when stimulus contrast was low. This result appears to depart from the prevailing view that NMDA receptor activation occurs secondary to nonNMDA-mediated depolarization and increased relief of the voltage-dependent Mg^{2+} block (Diamond & Copenhagen, 1993; Kerchner & Nicoll, 2008). However, it was hypothesized that reduced Mg^{2+} binding affinity, possibly mediated by receptors containing the GluN3 subunit, could account for the independent activation of the NMDA receptor near threshold (Buldyrev & Taylor, 2013). The results shown here for parasol cells are similar to these previous results in that the NMDA conductance may contribute a larger fraction to the total conductance near contrast threshold (Fig. 11) though the NMDA conductance does not dominate nor is it activated independently of the AMPA/kainate contribution. In addition, the NMDA contribution does not increase with increasing contrast or temporal frequency; rather the gain of the temporal–contrast sensitivity function appears to be mirrored by correspondingly large changes in the AMPA/kainate receptor-mediated conductance. Finally, at high stimulus temporal frequencies and contrast, the early peak in the AMPA/kainate relative to NMDA-mediated conductance supports the view that in parasol ganglion cells, depolarization is initiated principally by a fast increase in $G_{\mathrm{AMPA/Ka}}$.

Acknowledgments

We thank Beth Peterson for assistance with data management, preparing the illustrations and for technical assistance during all experiments. This study was supported by NIH grant EY06778 to D.M.D., Vision Training grant EY007031 to J.D.C., NIH grant RR00166 to the Tissue Distribution Program of the National Primate Research Center at the University of Washington, and an NEI Vision Core Grant EY01730. All experiments were performed in the laboratory of D.M.D. All experiments were conceived and designed by D.M.D. and J.D.C. Data were collected, analyzed, and interpreted by J.D.C., D.M.D., and O.S.P. Article text was originally drafted by D.M.D. and J.D.C., with contributions from O.S.P.

References

Abbott CJ, Percival KA, Martin PR, Grunert U. Amacrine and bipolar inputs to midget and parasol ganglion cells in marmoset retina. Visual Neuroscience. 2012; 29:157–168. [PubMed: 22564345]

Ascher P, Nowak L. The role of divalent cations in the N-methyl-D-aspartate responses of mouse central neurones in culture. The Journal of Physiology. 1988; 399:247–266. [PubMed: 2457089]

Borg-Graham LJ. The computation of directional selectivity in the retina occurs presynaptic to the ganglion cell. Nature Nueroscience. 2001; 4:176–183.

Boos R, Muller F, Wassle H. Actions of excitatory amino acids on brisk ganglion cells in the cat retina. Journal of Neurophysiology. 1990; 64:1368–1379. [PubMed: 1980925]

Bormann J, Hamill OP, Sakmann B. Mechanism of anion permeation through channels gated by glycine and gamma-aminobutyric acid in mouse cultured spinal neurones. The Journal of Physiology. 1987; 385:243–286. [PubMed: 2443667]

Buldyrev I, Puthussery T, Taylor WR. Synaptic pathways that shape the excitatory drive in an OFF retinal ganglion cell. Journal of Neurophysiology. 2012; 107:1795–1807. [PubMed: 22205648]

Buldyrev I, Taylor WR. Inhibitory mechanisms that generate centre and surround properties in ON and OFF brisk-sustained ganglion cells in the rabbit retina. The Journal of Physiology. 2013; 591:303–325. [PubMed: 23045347]

Cafaro J, Rieke F. Regulation of spatial selectivity by crossover inhibition. The Journal of Neuroscience. 2013; 33:6310–6320. [PubMed: 23575830]

Callaway EM. Structure and function of parallel pathways in the primate early visual system. The Journal of Physiology. 2005; 566:13–19. [PubMed: 15905213]

Cao D, Lee BB, Sun H. Combination of rod and cone inputs in parasol ganglion cells of the magnocellular pathway. Journal of Vision. 2010; 10:4. [PubMed: 20884499]

Cohen ED. Interactions of inhibition and excitation in the light-evoked currents of X type retinal ganglion cells. Journal of Neurophysiology. 1998; 80:2975–2990. [PubMed: 9862900]

Cohen ED. Light-evoked excitatory synaptic currents of X-type retinal ganglion cells. Journal of Neurophysiology. 2000; 83:3217–3229. [PubMed: 10848542]

Cohen ED, Miller RF. The role of NMDA and non-NMDA excitatory amino acid receptors in the functional organization of primate retinal ganglion cells. Visual Neuroscience. 1994; 11:317–332. [PubMed: 8003456]

Cohen ED, Zhou ZJ, Fain GL. Ligand-gated currents of alpha and beta ganglion cells in the cat retinal slice. Journal of Neurophysiology. 1994; 72:1260–1269. [PubMed: 7528793]

Cooper B, Sun H, Lee BB. Psychophysical and physiological responses to gratings with luminance and chromatic components of different spatial frequencies. Journal of the Optical Society of America. A, Optics, Image Science, and Vision. 2012; 29:A314–A323.

Crook JD, Davenport CM, Peterson BB, Packer OS, Detwiler PB, Dacey DM. Parallel ON and OFF cone bipolar inputs establish spatially coextensive receptive field structure of blue-yellow ganglion cells in primate retina. The Journal of Neuroscience. 2009a; 29:8372–8387. [PubMed: 19571128]

Crook JD, Manookin MB, Packer OS, Dacey DM. Horizontal cell feedback without cone type-selective inhibition mediates “red-green” color opponency in midget ganglion cells of the primate retina. The Journal of Neuroscience. 2011; 31:1762–1772. [PubMed: 21289186]

Crook, JD.; Packer, OS.; Troy, JB.; Dacey, DM. Synaptic mechanisms of color and luminance coding: Rediscovering the X-Y dichotomy in primate retinal ganglion cells. In: Chalupa, LM.; Werner, JS., editors. The New Visual Neurosciences. Cambridge, MA: MIT Press; 2013. p. 123-144.

Crook JD, Peterson BB, Packer OS, Robinson FR, Gamlin PD, Troy JB, Dacey DM. The smooth monostratified ganglion cell: evidence for spatial diversity in the Y-cell pathway to the lateral geniculate nucleus and superior colliculus in the macaque monkey. The Journal of Neuroscience. 2008a; 28:12654–12671. [PubMed: 19036959]

Crook JD, Peterson BB, Packer OS, Robinson FR, Troy JB, Dacey DM. Y-cell receptive field and collicular projection of parasol ganglion cells in macaque monkey retina. The Journal of Neuroscience. 2008b; 28:11277–11291. [PubMed: 18971470]

Crook JD, Troy JB, Packer OS, Vrieslander JD, Dacey DM. Contribution of excitatory and inhibitory conductances to receptive field structure in midget and parasol ganglion cells of macaque monkey retina. Journal of Vision. 2009b; 9(14):57.

Dacey DM, Brace S. A coupled network for parasol but not midget ganglion cells in the primate retina. Visual Neuroscience. 1992; 9:279–290. [PubMed: 1390387]

Dacey DM, Crook JD, Packer OS. Distinct synaptic mechanisms create parallel S-ON and S-OFF color opponent pathways in the primate retina. Visual Neuroscience. 2013 Epub July 29: 1–13.

Dacey DM, Packer OS, Diller LC, Brainard DH, Peterson BB, Lee BB. Center surround receptive field structure of cone bipolar cells in primate retina. Vision Research. 2000; 40:1801–1811. [PubMed: 10837827]

Dacey DM, Petersen MR. Dendritic field size and morphology of midget and parasol ganglion cells of the human retina. Proceedings of the National Academy of Sciences of the United States of America. 1992; 89:9666–9670. [PubMed: 1409680]

Dacey DM, Peterson BB, Robinson FR, Gamlin PD. Fireworks in the primate retina: In vitro photodynamics reveals diverse LGN-projecting ganglion cell types. Neuron. 2003; 37:15–27. [PubMed: 12526769]

Davenport CM, Detwiler PB, Dacey DM. Effects of pH buffering on horizontal and ganglion cell light responses in primate retina: Evidence for the proton hypothesis of surround formation. The Journal of Neuroscience. 2008; 28:456–464. [PubMed: 18184788]

Demb JB, Haarsma L, Freed MA, Sterling P. Functional circuitry of the retinal ganglion cell's nonlinear receptive field. The Journal of Neuroscience. 1999; 19:9756–9767. [PubMed: 10559385]

Demb JB, Zaghloul K, Haarsma L, Sterling P. Bipolar cells contribute to nonlinear spatial summation in the brisk-transient (Y) ganglion cell in mammalian retina. The Journal of Neuroscience. 2001; 21:7447–7454. [PubMed: 11567034]

Derrington AM, Lennie P. Spatial and temporal contrast sensitivities of neurones in lateral geniculate nucleus of macaque. The Journal of Physiology. 1984; 357:219–240. [PubMed: 6512690]

Diamond JS, Copenhagen DR. The contribution of NMDA and non-NMDA receptors to the light-evoked input-output characteristics of retinal ganglion cells. Neuron. 1993; 11:725–738. [PubMed: 8104431]

Enroth-Cugell C, Robson JG. The contrast sensitivity of retinal ganglion cells of the cat. The Journal of Physiology. 1966; 187:517–552. [PubMed: 16783910]

Fahrenfort I, Sjoerdsma T, Ripps H, Kamermans M. Cobalt ions inhibit negative feedback in the outer retina by blocking hemichannels on horizontal cells. Visual Neuroscience. 2004; 21:501–511. [PubMed: 15579217]

Fahrenfort I, Steijaert M, Sjoerdsam T, Vickers E, Ripps H, van Asselt J, Endeman D, Klooster J, Numan R, ten Eikelder H, von Gersdorff H, Kamermans M. Hemichannel-mediated and pH-based feedback from horizontal cells to cones in the vertebrate retina. PLoS One. 2009; 4:1–21.

Field G, Chichilnisky E. Information processing in the primate retina: Circuitry and coding. Annual Review of Neuroscience. 2007; 30:1–30.

Flores-Herr N, Protti DA, Wassle H. Synaptic currents generating the inhibitory surround of ganglion cells in the mammalian retina. The Journal of Neuroscience. 2001; 21:4852–4863. [PubMed: 11425912]

Frishman LJ, Linsenmeier RA. Effects of picrotoxin and strychnine on non-linear responses of Y-type cat retinal ganglion cells. The Journal of Physiology. 1982; 324:347–363. [PubMed: 7097604]

Grünert U. Distribution of GABA and glycine receptors on bipolar and ganglion cells in the mammalian retina. Microscopy Research and Technique. 2000; 50:130–140. [PubMed: 10891877]

Grünert U, Ghosh KK. Midget and parasol ganglion cells of the primate retina express the a1 subunit of the glycine receptor. Visual Neuroscience. 1999; 16:957–966. [PubMed: 10580731]

Grünert U, Haverkamp S, Fletcher EL, Wassle H. Synaptic distribution of ionotropic glutamate receptors in the inner plexi-form layer of the primate retina. The Journal of Comparative Neurology. 2002; 447:138–151. [PubMed: 11977117]

Hirasawa H, Kaneko A. pH changes in the invaginating synaptic cleft mediate feedback from horizontal cells to cone photoreceptors by modulating Ca2+ channels. The Journal of General Physiology. 2003; 122:657–671. [PubMed: 14610018]

Hochstein S, Shapley RM. Linear and nonlinear spatial subunits in Y cat retinal ganglion cells. The Journal of Physiology. 1976; 262:265–284. [PubMed: 994040]

Ichinose T, Lukasiewicz PD. Inner and outer retinal pathways both contribute to surround inhibition of salamander ganglion cells. The Journal of Physiology. 2005; 565:517–535. [PubMed: 15760938]

Jacoby RA, Marshak DW. Synaptic connections of DB3 diffuse bipolar cell axons in macaque retina. The Journal of Comparative Neurology. 2000; 416:19–29. [PubMed: 10578100]

Kalbaugh TL, Zhang J, Diamond JS. Coagonist release modulates NMDA receptor subtype contributions at synaptic inputs to retinal ganglion cells. The Journal of Neuroscience. 2009; 29:1469–1479. [PubMed: 19193893]

Kamermans M, Fahrenfort I, Schultz K, Janssen-Bienhold U, Sjoerdsma T, Weiler R. Hemichannel-mediated inhibition in the outer retina. Science. 2001; 292:1178–1180. [PubMed: 11349152]

Kaplan E, Benardete E. The dynamics of primate retinal ganglion cells. Progress in Brain Research. 2001; 134:17–34. [PubMed: 11702542]

Kaplan E, Lee BB, Shapley RM. New views of primate retinal function. Progress in Retinal and Eye Research. 1990; 9:273–336.

Kerchner GA, Nicoll RA. Silent synapses and the emergence of a postsynaptic mechanism for LTP. Nature Reviews. Neuroscience. 2008; 9:813–825. [PubMed: 18854855]

Kumar SS, Huguenard JR. Pathway-specific differences in subunit composition of synaptic NMDA receptors on pyramidal neurons in neocortex. The Journal of Neuroscience. 2003; 23:10074–10083. [PubMed: 14602822]

Lee BB. Visual pathways and psychophysical channels in the primate. The Journal of Physiology. 2011; 589:41–47. [PubMed: 20724364]

Lee BB, Martin PR, Grunert U. Retinal connectivity and primate vision. Progress in Retinal and Eye Research. 2010; 29:622–639. [PubMed: 20826226]

Lee BB, Martin PR, Valberg A. The physiological basis of heterochromatic flicker photometry demonstrated in the ganglion cells of the macaque retina. The Journal of Physiology. 1988; 404:323–347. [PubMed: 3253435]

Lee BB, Pokorny J, Smith VC, Martin PR, Valberg A. Luminance and chromatic modulation sensitivity of macaque ganglion cells and human observers. Journal of the Optical Society of America. 1990; 7:2223–2236. [PubMed: 2090801]

Lee BB, Sun H, Zucchini W. The temporal properties of the response of macaque ganglion cells and central mechanisms of flicker detection. Journal of Vision. 2007; 7:11–116.

Lennie P, Movshon JA. Coding of color and form in the geniculostriate visual pathway (invited review). Journal of the Optical Society of America. A, Optics, Image Science, and Vision. 2005; 22:2013–2033.

Leventhal AG, Rodieck RW, Dreher B. Retinal ganglion cell classes in the old world monkey: Morphology and central projections. Science. 1981; 213:1139–1142. [PubMed: 7268423]

Lin B, Martin PR, Solomon SG, Grunert U. Distribution of glycine receptor subunits on primate retinal ganglion cells: a quantitative analysis. The European Journal of Neuroscience. 2000; 12:4155–4170. [PubMed: 11122328]

Macri J, Martin PR, Grunert U. Distribution of the alpha1 subunit of the GABA(A) receptor on midget and parasol ganglion cells in the retina of the common marmoset Callithrix jacchus. Visual Neuroscience. 2000; 17:437–448. [PubMed: 10910110]

Manookin MB, Beaudoin DL, Ernst ZR, Flagel LJ, Demb JB. Disinhibition combines with excitation to extend the operating range of the OFF visual pathway in daylight. The Journal of Neuroscience. 2008; 28:4136–4150. [PubMed: 18417693]

Manookin MB, Weick M, Stafford BK, Demb JB. NMDA receptor contributions to visual contrast coding. Neuron. 2010; 67:280–293. [PubMed: 20670835]

Massey SC, Miller RF. *N*-methyl-D-aspartate receptors of ganglion cells in rabbit retina. Journal of Neurophysiology. 1990; 63:16–30. [PubMed: 2153770]

McMahon MJ, Packer OS, Dacey DM. The classical receptive field surround of primate parasol ganglion cells is mediated primarily by a non-GABAergic pathway. The Journal of Neuroscience. 2004; 24:3736–3745. [PubMed: 15084653]

Mittman S, Taylor WR, Copenhagen DR. Concomitant activation of two types of glutamate receptor mediates excitation of salamander retinal ganglion cells. The Journal of Physiology. 1990; 428:175–197. [PubMed: 2172521]

Molnar A, Hsueh HA, Roska B, Werblin FS. Crossover inhibition in the retina: Circuitry that compensates for nonlinear rectifying synaptic transmission. Journal of Computational Neuroscience. 2009; 27:569–590. [PubMed: 19636690]

Monyer H, Burnashev N, Laurie DJ, Sakmann B, Seeburg PH. Developmental and regional expression in the rat brain and functional properties of four NMDA receptors. Neuron. 1994; 12:529–540. [PubMed: 7512349]

Murphy GJ, Rieke F. Network variability limits stimulus-evoked spike timing precision in retinal ganglion cells. Neuron. 2006; 52:511–524. [PubMed: 17088216]

Packer OS, Verweij J, Li PH, Schnapf JL, Dacey DM. Blue-yellow opponency in primate S cone photoreceptors. The Journal of Neuroscience. 2010; 30:568–572. [PubMed: 20071519]

Paoletti P. Molecular basis of NMDA receptor functional diversity. The European Journal of Neuroscience. 2011; 33:1351–1365. [PubMed: 21395862]

Peichl L. Alpha ganglion cells in mammalian retinae: Common properies, species differences, and some comments on other ganglion cells. Visual Neuroscience. 1991; 7:155–169. [PubMed: 1931799]

Perry VH, Oehler R, Cowey A. Retinal ganglion cells that project to the dorsal lateral geniculate nucleus in the macaque monkey. Neuroscience. 1984; 12:1101–1123. [PubMed: 6483193]

Pokorny J, Smithson H, Quinlan J. Photostimulator allowing independent control of rods and the three cone types. Visual Neuroscience. 2004; 21:263–267. [PubMed: 15518198]

Sagdullaev BT, McCall MA, Lukasiewicz PD. Presynaptic inhibition modulates spillover, creating distinct dynamic response ranges of sensory output. Neuron. 2006; 50:923–935. [PubMed: 16772173]

Schwartz GW, Okawa H, Dunn FA, Morgan JL, Kerschensteiner D, Wong RO, Rieke F. The spatial structure of a nonlinear receptive field. Nature Neuroscience. 2012; 15:1572–1580. [PubMed: 23001060]

Shapley R, Perry VH. Cat and monkey retinal ganglion cells and their visual functional roles. Trends Neuroscience. 1986; 9:229–235.

Silveira LC, Saito CA, Lee BB, Kremers J, da Silva Filho M, Kilavik BE, Yamada ES, Perry VH. Morphology and physiology of primate M- and P-cells. Progress in Brain Research. 2004; 144:21–46. [PubMed: 14650838]

Solomon SG, Martin PR, White AJ, Ruttiger L, Lee BB. Modulation sensitivity of ganglion cells in peripheral retina of macaque. Vision Research. 2002; 42:2893–2898. [PubMed: 12450500]

Spitzer H, Hochstein S. Simple- and complex-cell response dependences on stimulation parameters. Journal of Neurophysiology. 1985; 53:1244–1265. [PubMed: 3998808]

Taylor WR. TTX attenuates surround inhibition in rabbit retinal ganglion cells. Visual Neuroscience. 1999; 16:285–290. [PubMed: 10367963]

Taylor WR, Vaney DI. Diverse synaptic mechanisms generate direction selectivity in the rabbit retina. Journal of Neuroscience. 2002; 22(17):7712–7720. [PubMed: 12196594]

Thoreson WB, Mangel SC. Lateral interactions in the outer retina. Progress in Retinal and Eye Research. 2012; 31:407–441. [PubMed: 22580106]

van Wyk M, Wassle H, Taylor WR. Receptive field properties of ON- and OFF-ganglion cells in the mouse retina. Visual Neuroscience. 2009; 26:297–308. [PubMed: 19602302]

Velte TJ, Yu W, Miller RF. Estimating the contributions of NMDA and non-NMDA currents to EPSPs in retinal ganglion cells. Visual Neuroscience. 1997; 14:999–1014. [PubMed: 9447684]

Venkataramani S, Taylor WR. Orientation selectivity in rabbit retinal ganglion cells is mediated by presynaptic inhibition. The Journal of Neuroscience. 2010; 30:15664–15676. [PubMed: 21084622]

Verweij J, Hornstein EP, Schnapf JL. Surround antagonism in macaque cone photoreceptors. The Journal of Neuroscience. 2003; 23:10249–10257. [PubMed: 14614083]

Verweij J, Kamermans M, Spekreijse H. Horizontal cells feed back to cones by shifting the cone calcium-current activation range. Vision Research. 1996; 36:3943–3953. [PubMed: 9068848]

Victor JD, Shapley RM. The nonlinear pathway of Y ganglion cells in the cat retina. The Journal of General Physiology. 1979; 74:671–687. [PubMed: 231636]

Vigh J, Witkovsky P. Sub-millimolar cobalt selectively inhibits the receptive field surround of retinal neurons. Visual Neuroscience. 1999; 16:159–168. [PubMed: 10022487]

Watanabe M, Rodieck RW. Parasol and midget ganglion cells of the primate retina. The Journal of Comparative Neurology. 1989; 289:434–454. [PubMed: 2808778]

Werblin FS. Six different roles for crossover inhibition in the retina: correcting the nonlinearities of synaptic transmission. Visual Neuroscience. 2010; 27:1–8. [PubMed: 20392301]

Werblin FS. The retinal hypercircuit: a repeating synaptic interactive motif underlying visual function. The Journal of Physiology. 2011; 589:3691–3702. [PubMed: 21669978]

Wyllie DJ, Livesey MR, Hardingham GE. Influence of GluN2 subunit identity on NMDA receptor function. Neuropharmacology. 2013; 74:4–17. [PubMed: 23376022]

Zeck GM, Xiao Q, Masland RH. The spatial filtering properties of local edge detectors and brisk-sustained retinal ganglion cells. The European Journal of Neuroscience. 2005; 22:2016–2026. [PubMed: 16262640]

Zhang J, Diamond JS. Subunit- and pathway-specific localization of NMDA receptors and scaffolding proteins at ganglion cell synapses in rat retina. The Journal of Neuroscience. 2009; 29:4274–4286. [PubMed: 19339621]

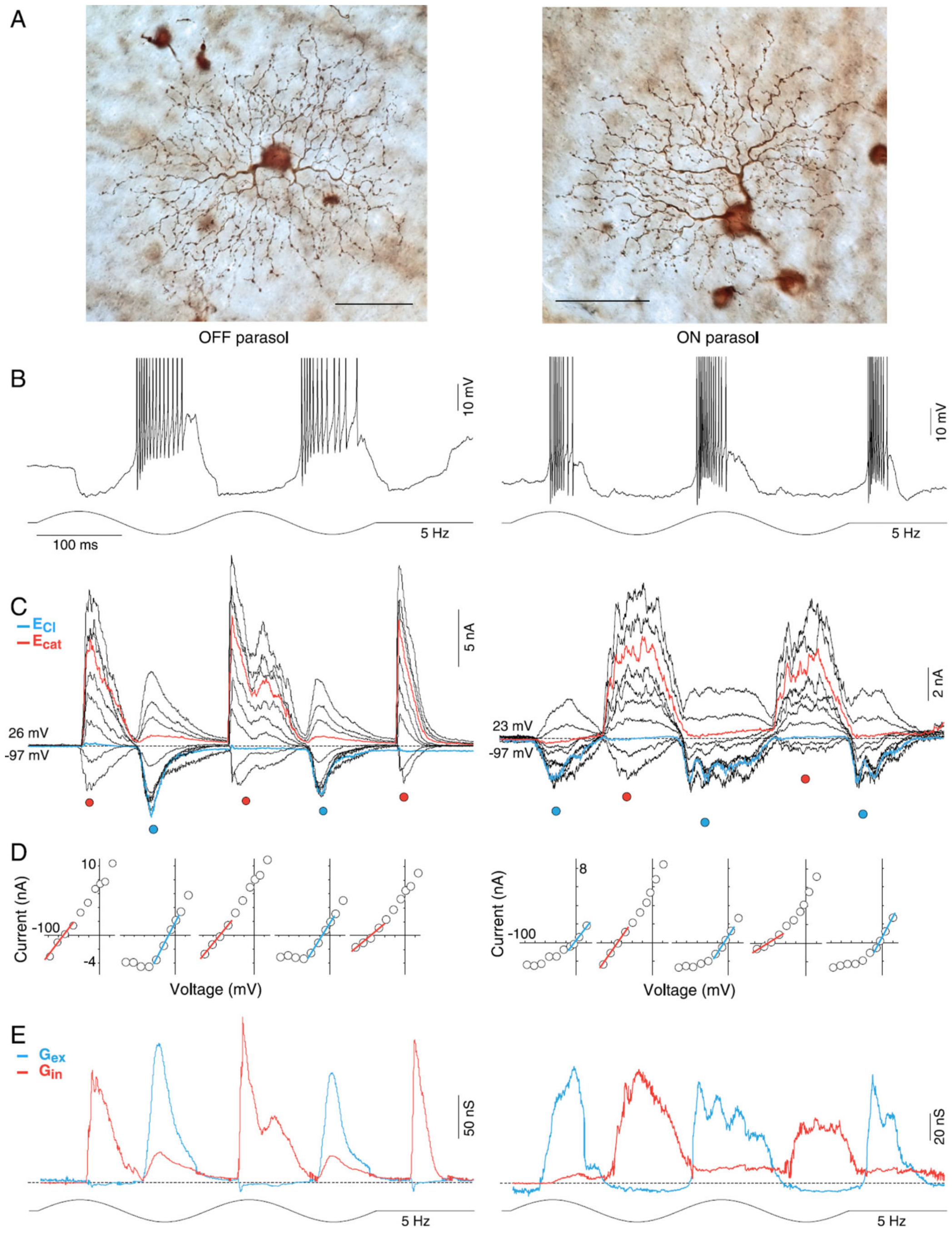

Fig. 1.

OFF and ON parasol cell light-evoked excitatory and crossover inhibitory synaptic conductances are largely rectified. (**A**) Dendritic morphology of OFF (left panel) and ON (right panel) parasol cells in the near retinal periphery (~5 mm eccentric from fovea). OFF and ON cells have relatively large somas and moderately branched, spine-laden dendritic trees that permit reliable targeting and identification in the *in vitro* retina. Scale bar = 50 µm (**B**) Intracellular voltage response (current clamp mode) from OFF (left) and ON (right) parasol cells to a large stimulus field (1-mm diameter 100% contrast, sinusoidally modulated at 5 Hz, two stimulus cycles shown; effective quanta ~1.1 × 10^5 photons/s/μm^2). The membrane potential depolarizes (spikes have been partially clipped to permit enlargement of membrane potential) and hyperpolarizes in-phase with light decrement and increment respectively for the OFF cell, and conversely for the ON cell. (**C**) Family of light-evoked postsynaptic currents for an OFF (left) and ON (right) parasol cell in response to the same stimulus as shown in *B* for ten holding potentials ranging from approximately −90 to +40 mV at ~15 mV intervals. Currents evoked near the chloride (−65 mV) and cation (0 mV) equilibrium potentials are indicated in blue and red, respectively. (**D**) Current-voltage (*I*–*V*) plots for time points at peak increment and decrement of stimulus indicated by red- and blue-filled circles below the current traces in (**B**). Reversal potential and slope were determined from linear fits (red and blue lines) to data points around the reversal potential. (**E**) Excitatory (blue) and inhibitory (red) synaptic conductances derived from slope and reversal potential of linear fits to *I*—*Vs* at 1.5-ms intervals across two stimulus cycles (see Materials and methods for details). Note that for both ON and OFF parasol cells, a rectified excitatory conductance underlies membrane depolarization during spiking phase of the light response and a very large and similarly rectified inhibitory conductance (“crossover inhibition”) is present during the hyperpolarizing response phase.

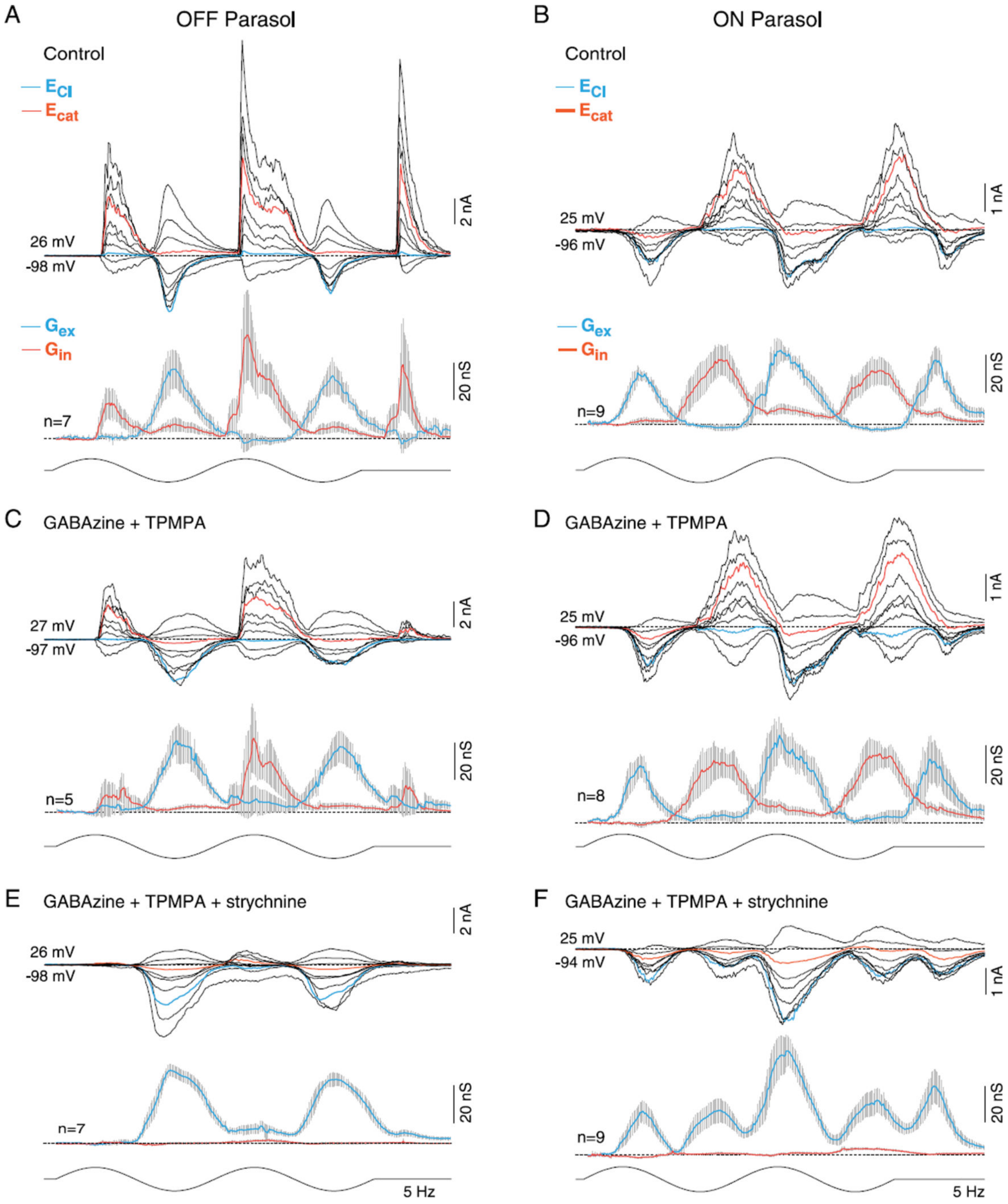

Fig. 2.

Effect of $GABA_A$, $GABA_C$, and glycine receptor antagonists on light-evoked synaptic conductances in OFF- and ON-center parasol cells. (**A** and **B**) Upper traces: family of light evoked synaptic currents for an OFF- (**A**) and ON-center (**B**) parasol cell; stimulus 50% contrast; other conventions as given in Fig. 1. Lower traces: mean (gray shading indicates s.e.), excitatory (blue), and inhibitory (red) synaptic conductances; conventions as given in Fig. 1. (**C** and **D**), as in (**A** and **B**) after bath application of $GABA_A$ (GABAzine; 5 μM) and $GABA_C$ (TPMPA; 50 μM) receptor antagonists. There were no significant changes in the contribution of the feedforward inhibition (control *vs*. block of $GABA_A$ and $GABA_C$ receptors: OFF cells 9 ± 4 *vs*. 2 ± 1 nS and ON cells 8 ± 2 *vs*. 10 ± 3 nS), crossover inhibition (OFF cells 61 ± 23 *vs*. 47 ± 18 nS and ON cells 35 ± 7 *vs*. 37 ± 6 nS) or the excitatory conductance (OFF cells 41 ± 9 *vs*. 46 ± 7 nS and ON cells 40 ± 5 *vs*. 47 ± 9 nS). (**E** and **F**) As in (**C** and **D**) after addition of glycine receptor antagonist to bath (strychnine, 1 μM). Strychnine abolishes all crossover inhibition, significantly increases the existing excitatory response (control *vs*. GABA plus glycine receptor block: OFF cells, 41 ± 9 *vs*. 60 ± 5 and ON cells, 40 ± 5 *vs*. 58 ± 8 nS), and unmasks a small and large crossover excitatory conductance in OFF (13 ± 4 nS) and ON parasol cells (28 ± 5 nS), respectively.

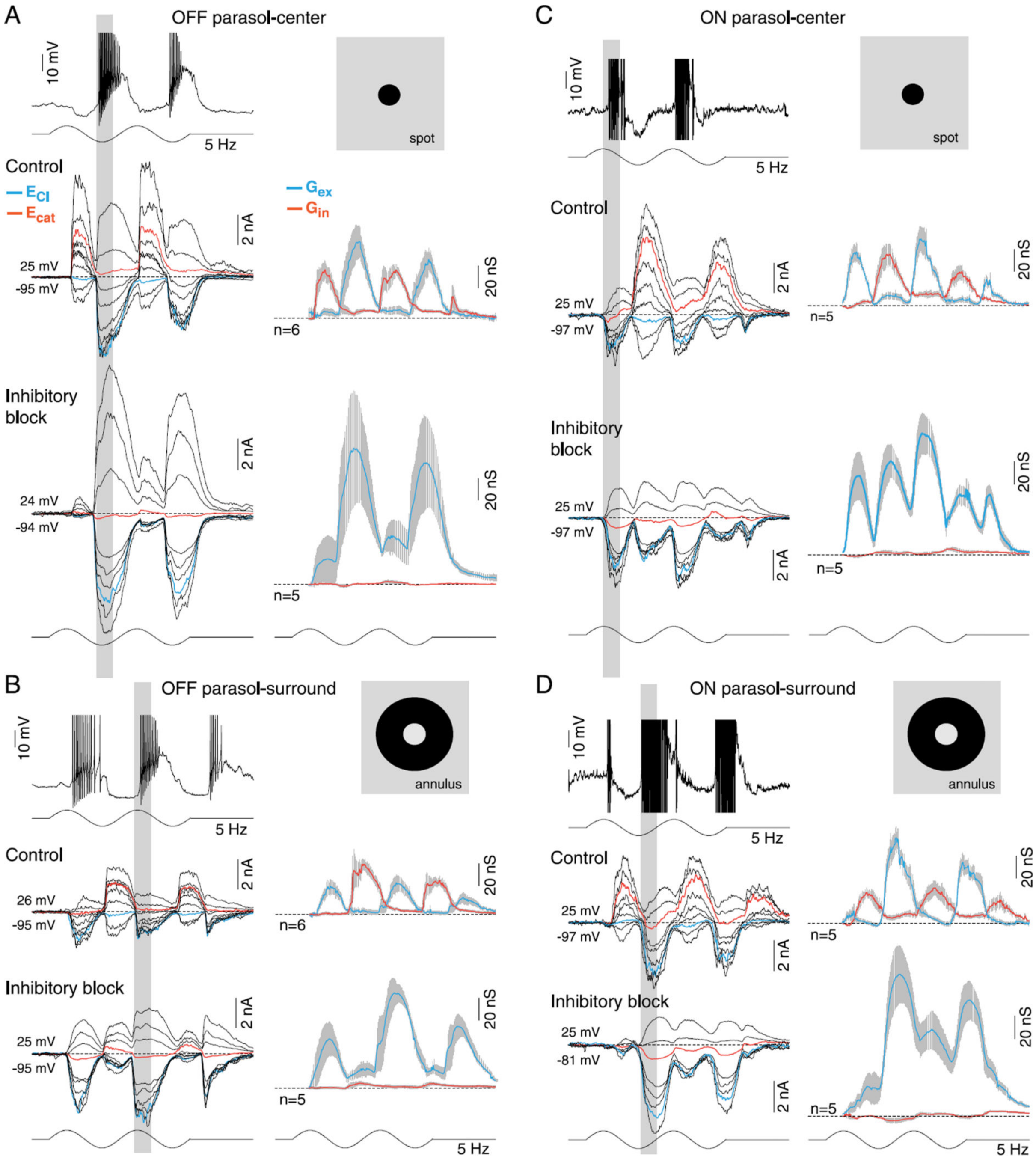

Fig. 3.

Synaptic inhibition is not required for center–surround antagonism in OFF- and ON-center parasol cells. (**A-D**) Current and voltage clamp recordings from OFF- and ON-center parasol cells in response to a spot (**A, C**; 100-μm diameter) or annulus (**B, D**; 100-μm inner diameter) modulated at 5 Hz, 100% contrast, as indicated by the spot and annulus inset icons (effective quanta ~2.5×10^5 photons/s/μm^2). Current clamp intracellular recording (**A, D**, top traces) shows that spike discharge and membrane potential modulation in response to spot *versus* annuli are ~180 out of phase (indicted by the vertical gray-shaded bars), demonstrating strong center–surround antagonism in both ON and OFF cells. (**A** and **C**) Middle traces, family of light-evoked synaptic currents for an OFF- (**A**) and ON-center (**C**) cell in response to a spot; mean (gray shading, s.e.), excitatory (G_{ex}, blue), and inhibitory (G_{in}, red) conductances for sample number indicated are shown to the right of current family. (**A** and **C**) Lower traces, synaptic currents, and conductances after application of GABA_A (GABAzine, 5 μM), GABA_C (TPMPA, 50 μM), and glycine (strychnine, 1 μM) receptor antagonists. OFF parasol cell peak excitation increased from 69 ± 14 to 124 ± 53 nS and ON parasol cell peak excitation from 62 ± 11 to 107 ± 20 nS. (**B** and **D**) Middle and lower traces as in (**A**), (**C**) but responses to a surround isolating annulus are shown for the same sample of cells. Note that both the excitatory and inhibitory conductances reverse phase in response to stimulation with spot *versus* annulus (as indicated by the gray-shaded vertical bars). Note also that for both ON and OFF cells, the surround-mediated excitatory conductance persists and increases in amplitude after the block of synaptic inhibition. Total excitation is increased in both OFF-center (31 ± 7 *vs*. 89 ± 14 nS) and ON-center cells (80 ± 9 *vs*. 122 ± 25 nS) after the block of synaptic inhibition, with the addition of crossover excitation (see Fig. 2) especially evident in the ON parasol cell.

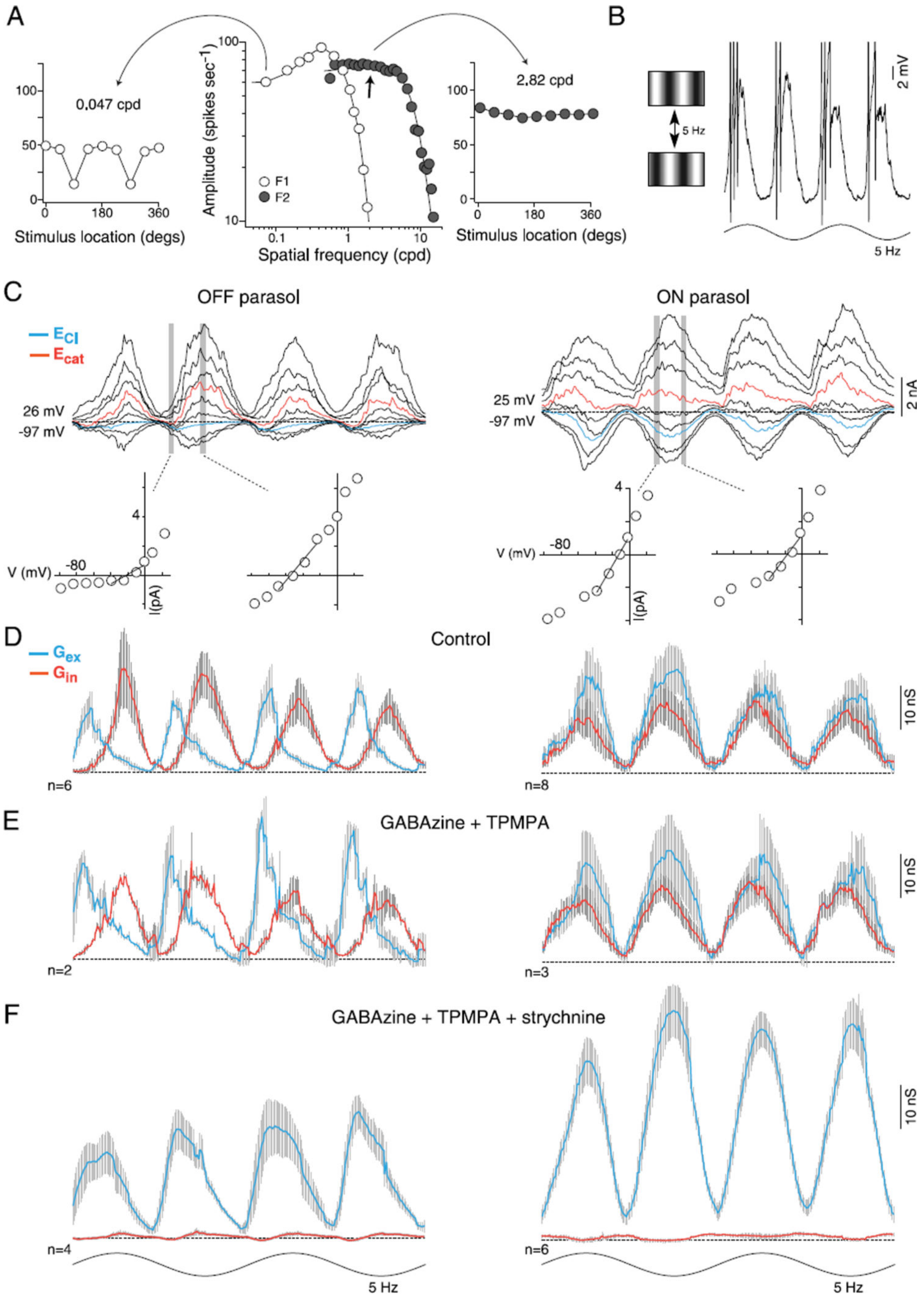

Fig. 4.

Synaptic inhibition is not required for the parasol cell frequency-doubled response to stimuli of high spatial frequency (the “Y-cell signature”). (**A**) Middle, spatial frequency tuning of an OFF parasol cell; open circles plot spike discharge in response to drifting grating varied in spatial frequency (cpd, cycles/deg of visual angle), and modulated sinusoidally in contrast (5 Hz, 50% contrast; first harmonic amplitude, F1). F1 response is fit with a difference-of-Gaussians center–surround receptive field model (center diameter = 111 μm). Filled circles plot second harmonic (“frequency-doubled,” F2) amplitude to stationary gratings that reverse in contrast (5 Hz, 50% contrast). F2 response is fit with a single Gaussian (center diameter = 31 µm). Either side of the spatial tuning curves are F1 (left) and F2 (right) responses to contrast-reversing gratings of 0.047 cpd (left) and 2.82 cpd (right) as a function of the location of the stimulus relative to the receptive field center (degrees). At 0.047 cpd, F1 dominates and is sensitive to the location of the stimulus (90 and 270 deg), whereas to a finer spatial frequency (2.82 cpd, right), F2 dominates regardless of the location of the stimulus. (**B**) Left, cartoon of the contrast reversing grating stimulus. Right, intracellular current clamp recording of an OFF cell near the peak of the F2 spatial frequency response (arrow in the middle plot in **A**). Membrane potential deeply modulates at twice the stimulus frequency. (**C**) Family of frequency-doubled synaptic currents evoked to contrast reversing gratings at the peak of the spatial frequency response for an OFF (left) and ON parasol cell (right). *I—V* plots at two time points indicated by vertical gray bars shown below synaptic currents. (**D**) Average excitatory (G_{ex}, blue) and inhibitory (G_{in}, red) synaptic conductances for 6 OFF- (left) and 8 ON- (right) center cells. (**E**) Addition of $GABA_A$ ($GABA_{zine}$, 5 µM) and $GABA_C$ (TPMPA, 50 µM) receptor antagonists; average conductance as indicated in (**C**). OFF cell peak of the excitatory conductance increased from 17 ± 2 to 28 ± 2 nS while peak crossover inhibition showed little change (20 ± 3 to 17 ± 1 nS). ON parasol cells: the peak excitation (22 ± 3 to 25 ± 4 nS) and inhibition (16 ± 2 to 18 ± 1) showed little change. (**F**) Addition of the glycine receptor antagonist strychnine (1 µM) eliminates the inhibitory synaptic conductance; frequency doubled synaptic excitation is preserved and total excitation is increased in both OFF- (25 ± 2 nS) and ON-center cells (48 ± 3 nS).

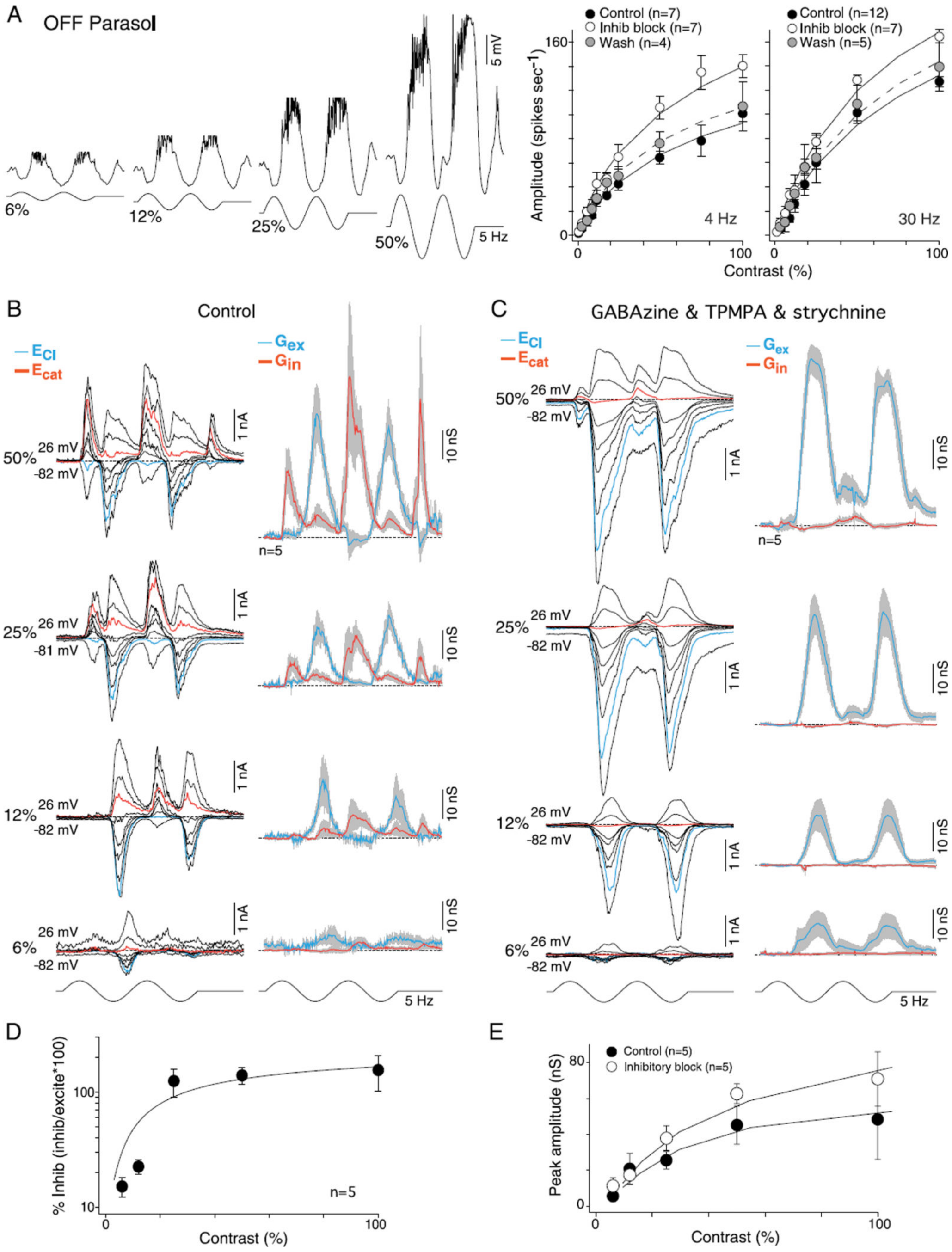

Fig. 5.

Contrast sensitivity of excitatory and inhibitory conductances for OFF-center parasol cells: high sensitivity is mediated by synaptic excitation. (**A**) Left, intracellular voltage recording of an OFF-parasol to 6, 12, 25, and 50% sinusoidal contrast modulation (5 Hz, 1-mm field diameter). Membrane potential depolarizes during OFF-phase and hyperpolarizes during ON-phase (spikes removed for illustrative purposes). Right, plots of spike rate as a function of stimulus contrast (first harmonic amplitude) for 4- and 30-Hz stimulus temporal frequencies before (solid circles) and after application of $GABA_A$ (GABAzine, 5 μM) and

$\mathrm{GABA_C}$ (TPMPA, 50 μM) and glycine (strychnine; 1 μM) receptor antagonists (open circles). Solid lines are Naka-Rushton fits (4Hz: control s_e = 0.8, inhibitory block s_e = 1.0, and wash s_e = 0.8; 30 Hz: control s_e = 2.3, inhibitory block s_e = 1.7, and wash s_e = 2.0; see Materials and methods). Contrast gain values increase for the 4-Hz responses (control 2.7 ± 1.2, inhibitory block 4.7 ± 3.0, and wash 2.8 ± 0.6) and 30-Hz responses (control 3.3 ± 1.3, inhibitory block 4.6 ± 1.9, and wash 3.7 ± 1.9). (**B**) Left, family of light-evoked synaptic currents (stimulus as in **A**) for a single OFF-parasol at 6, 12, 25, and 50% contrast. Right, average excitatory (blue) and inhibitory (red) synaptic conductances for five cells (conventions as in Figs. 2 and 3). (**C**) Data shown as in (**B**) after the block of GABAergic and glycinergic inhibition, as in (**A**); excitatory conductances persist at all contrasts and increase in amplitude. (**D**) Plot of peak mean inhibitory conductance relative to excitatory conductance [peak inhibition/peak (excitation + inhibition)]. Percent of synaptic inhibition was calculated on a cell-by-cell basis. Inhibition is greatly reduced relative to excitation at lower contrasts. Solid line is a Naka-Rushton fit (s_e = 11.4). (**E**) Peak excitatory conductances before (solid circles) and after (open circles) the addition of GABA and glycine receptor antagonists plotted as a function of contrast. Solid lines are Naka-Rushton fits (control s_e = 1.8 and inhibitory block s_e = 2.0). Contrast gain increases from 1.4 ± 0.3 to 2.5 ± 0.6.

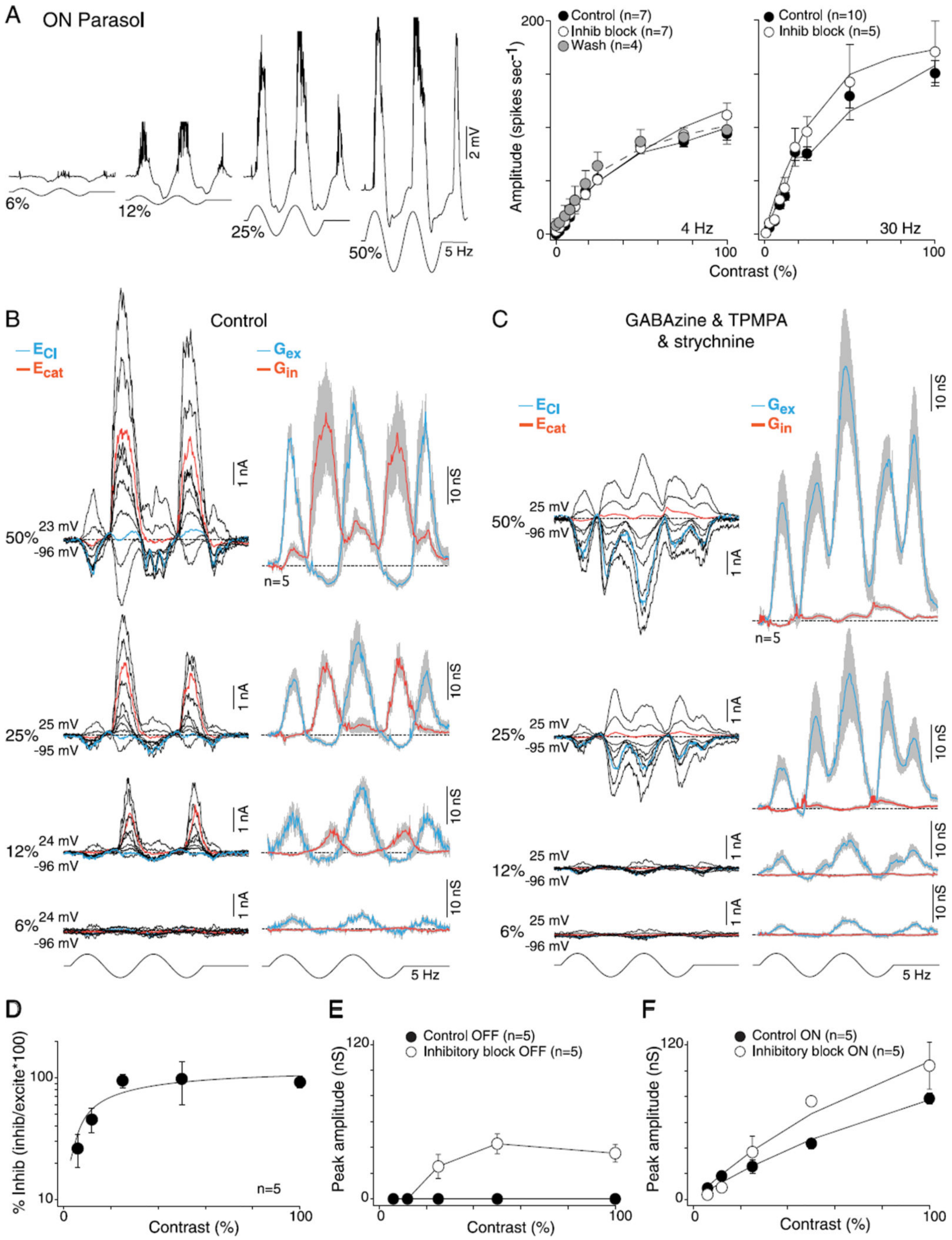

Fig. 6.

Contrast sensitivity of excitatory and inhibitory conductances for ON-center parasol cells: high sensitivity is mediated by synaptic excitation. (**A**) Left, intracellular voltage recording of an ON-parasol to 6, 12, 25, and 50% sinusoidal contrast modulation (5 Hz, 1-mm field diameter). Membrane potential depolarizes during ON-phase and hyperpolarizes during OFF-phase (spikes removed for illustrative purposes). Right, plots of spike rate as a function of stimulus contrast (first harmonic amplitude) for 4- and 30-Hz stimulus temporal frequencies before (solid circles) and after (open circles) application of $GABA_A$

(GABAzine, 5 μM) and GABA$_C$ (TPMPA, 50 μM) and glycine (strychnine, 1 μM) receptor antagonists. Solid lines are Naka–Rushton fits (4Hz: control s_e = 1.4, inhibitory block s_e = 0.9, and wash s_e = 1.4; 30 Hz: control s_e = 3.1 and inhibitory block s_e = 4.7). Contrast gain values increase for the 4-Hz (control 2.7 ± 0.7, inhibitory block 2.9 ± 1.3, and wash 4.3 ± 1.8) and 30-Hz responses (control 4.0 ± 1.1 and inhibitory block 5.8 ± 2.3). (**B**) Left, family of light-evoked synaptic currents (stimulus as in **A**) for a single ON-parasol at 6, 12, 25, and 50% contrast. Right, average excitatory (blue) and inhibitory (red) synaptic conductances for five cells (other conventions as in Figs. 2 – 5). (**C**) Data shown as in (**B**) after the block of GABAergic and glycinergic inhibition, as in (**A**). Excitatory conductances persist at all contrasts and increase in amplitude. (**D**) Plot of the peak mean inhibitory conductance relative to excitatory conductance [peak inhibition/peak (excitation + inhibition)]. Percent of synaptic inhibition was calculated on a cell-by-cell basis. Inhibition is greatly reduced relative to excitation at lower contrasts. Solid line is a Naka–Rushton fit (s_e = 5.9). (**E**) Peak unmasked excitation before (solid circles) and after (open circles) the addition of GABA and glycine receptor antagonists plotted as a function of contrast. Solid lines connect the data points. (**F**) Peak ON excitatory conductances before (solid circles) and after (open circles) the addition of GABA and glycine receptor antagonists plotted as a function of contrast. Solid lines are Naka–Rushton fits (control s_e = 1.4 and inhibitory block s_e =3.3). Contrast gain increases from 1.4 ± 0.2 to 2.0 ± 0.4.

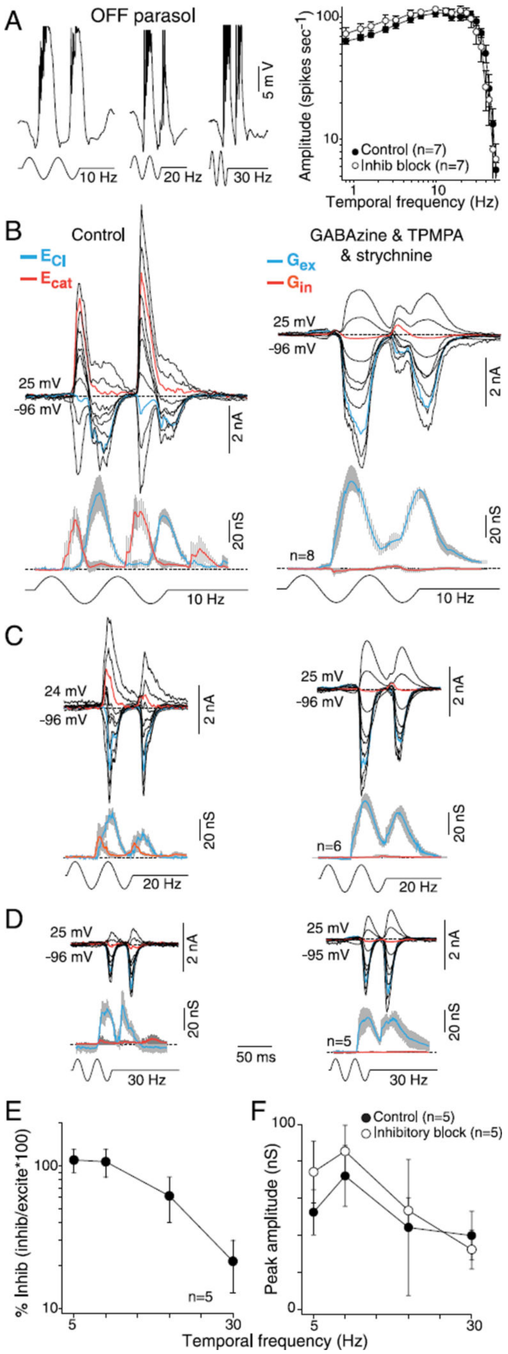

Fig. 7.

Temporal tuning of excitatory and inhibitory conductances for OFF-center parasol cells: high sensitivity is mediated by synaptic excitation. (**A**) Left, intracellular voltage recording of an OFF-parasol to 10-, 20-, and 30-Hz temporal frequency modulation (50% contrast, 1-mm stimulus diameter). Membrane potential depolarizes during OFF-phase and hyper-polarizes during ON-phase after a latency to a stimulus onset of ~35 ms (spikes removed for illustrative purposes). Right, a plot of spike rate as a function of stimulus temporal frequency (50% contrast; 1-mm stimulus diameter; first harmonic amplitude) before (solid circles) and after (open circles) application of GABA_A (GABAzine, 5 μM) and GABA_C (TPMPA, 50 μM) and glycine (strychnine; 1 μM) receptor antagonists. (**B**–**D**) Family of stimulus-evoked synaptic currents to 10 Hz (**B**), 20 Hz (**C**) and 30 Hz (**D**) temporal modulation before (upper left) and after (upper right) the addition of GABAzine, TPMPA, and strychnine. Lower left and right, mean excitatory (blue) and inhibitory (red) synaptic conductances derived from sample number indicated for each associated stimulus condition. (**E**) Plot of percentage peak crossover inhibitory relative to excitatory conductance [peak inhibition/peak (excitation + inhibition)] as a function of temporal frequency. Percent of synaptic inhibition was calculated on a cell-by-cell basis. Crossover inhibition declines with increasing temporal frequency and is largely absent at 30 Hz, the highest temporal frequency measured. (**F**) Average peak OFF conductances before (solid circles) and after (open circles) the block of synaptic inhibition plotted as a function of temporal frequency.

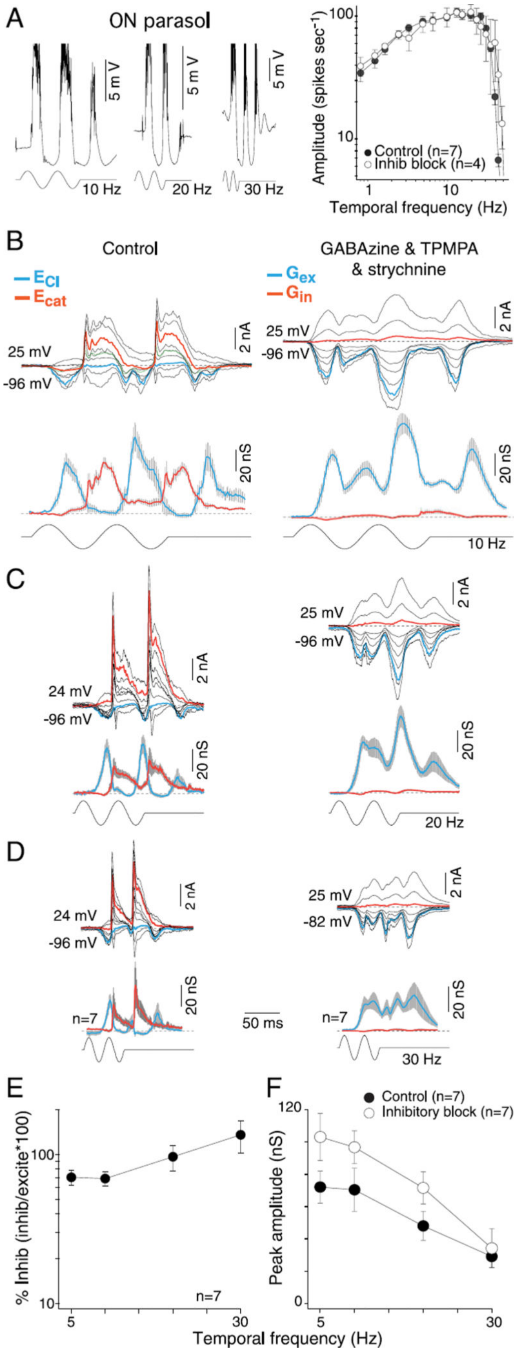

Fig. 8.

Temporal tuning of excitatory and inhibitory conductances for ON-center parasol cells: high sensitivity is mediated by synaptic excitation. (**A**) Left, intracellular voltage recording of an ON-parasol to 10-, 20-, and 30-Hz temporal frequency modulation (50% contrast, 1-mm stimulus diameter). Membrane potential depolarizes during ON-phase and hyperpolarizes during OFF-phase after a latency to stimulus onset of ~35 ms (spikes removed for illustrative purposes). Right, plots of spike rate as a function of stimulus temporal frequency (50% contrast; 1-mm stimulus diameter; first harmonic amplitude) before (solid circles) and after (open circles) application of GABA$_A$(GABAzine, 5 μM) and GABA$_C$ (TPMPA, 50 μM) and glycine (strychnine; 1 μM) receptor antagonists. (**B–D**) Family of stimulus-evoked synaptic currents to 10 Hz (**B**), 20 Hz (**C**), and 30 Hz (**D**) temporal modulation before (upper left) and after (upper right) the addition of GABAzine, TPMPA, and strychnine. Lower left and right, mean excitatory (blue) and inhibitory (red) synaptic conductances derived from sample number indicated for each associated stimulus condition. (**E**) Plot of percentage peak inhibitory conductance relative to excitatory conductance [peak inhibition/peak (excitation + inhibition)] as a function of temporal frequency. Percent of synaptic inhibition was calculated on a cell-by-cell basis. Crossover inhibitory conductance is maintained and increases relative to excitatory conductance with increasing temporal frequency. (**F**) Average peak ON conductances before (solid circles) and after (open circles) the block of synaptic inhibition plotted as a function of temporal frequency.

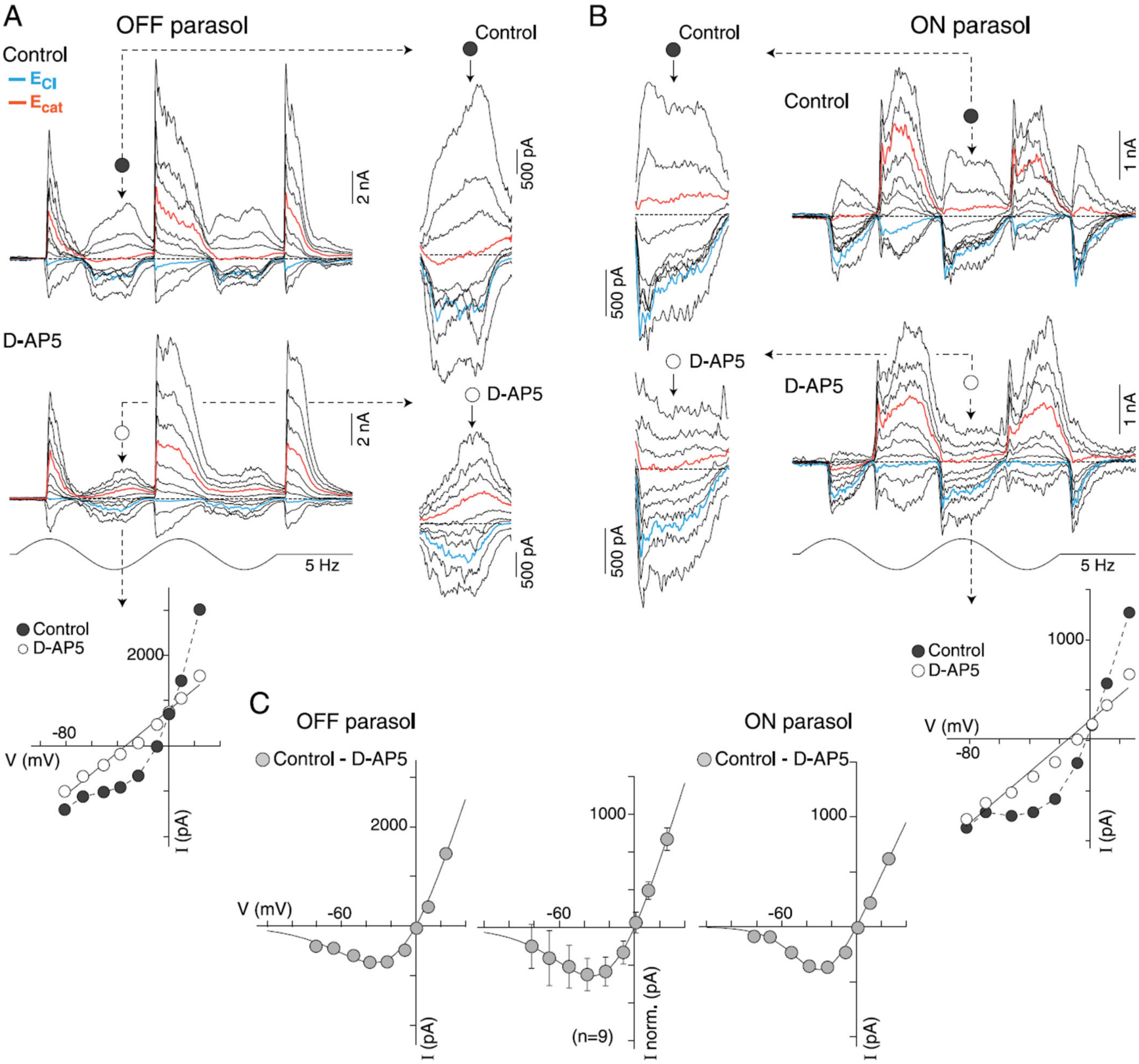

Fig. 9.

Application of D-AP5 linearizes the current-voltage relationship of excitatory synaptic currents and reveals similar NMDA receptor-mediated synaptic currents in both OFF and ON parasol cells. (**A** and **B**) Family of light-evoked synaptic currents (5 Hz, 2 stimulus cycles, 50% contrast, 1-mm stimulus diameter, effective quanta $\sim 1.1 \times 10^{5}$photons/s/μm^{2}) from an OFF- (**A**) and an ON-center (**B**) parasol before (control, upper trace family) and after (lower trace family) application of NMDA receptor antagonist, D-AP5 (50 μM). Insets (indicated by dotted arrows) show enlargement of excitatory response phase (decrement for OFF cells, increment for ON cells) for all traces currents near E_{Cl} and E_{cat} indicated in blue and red, respectively. Nonlinearity at negative holding potentials is evident in traces and is greatly reduced after D-AP5 application. Plots below traces show I–V relationship in control (filled circles) and after D-AP5 (open circles) at a time point indicated by a dotted arrow. (**C**) Plot of subtraction of D-AP5 from control *I*–*V* gives an estimate of NMDA-mediated *I*–*V* relationship for the OFF (left plot) and ON (right plot) cell examples. Plot at center shows average *I*–*V* for 9 parasol cells (6 OFF and 3 ON cells; error bars ± S.D.). Data for the individual and averaged *I*–*V* s are least squares fit with a function that describes the voltage dependence of the NMDA receptor conductance (K_{Mg} = 3.5 mM and V_{δ} = 22 mV; see Materials and methods for details).

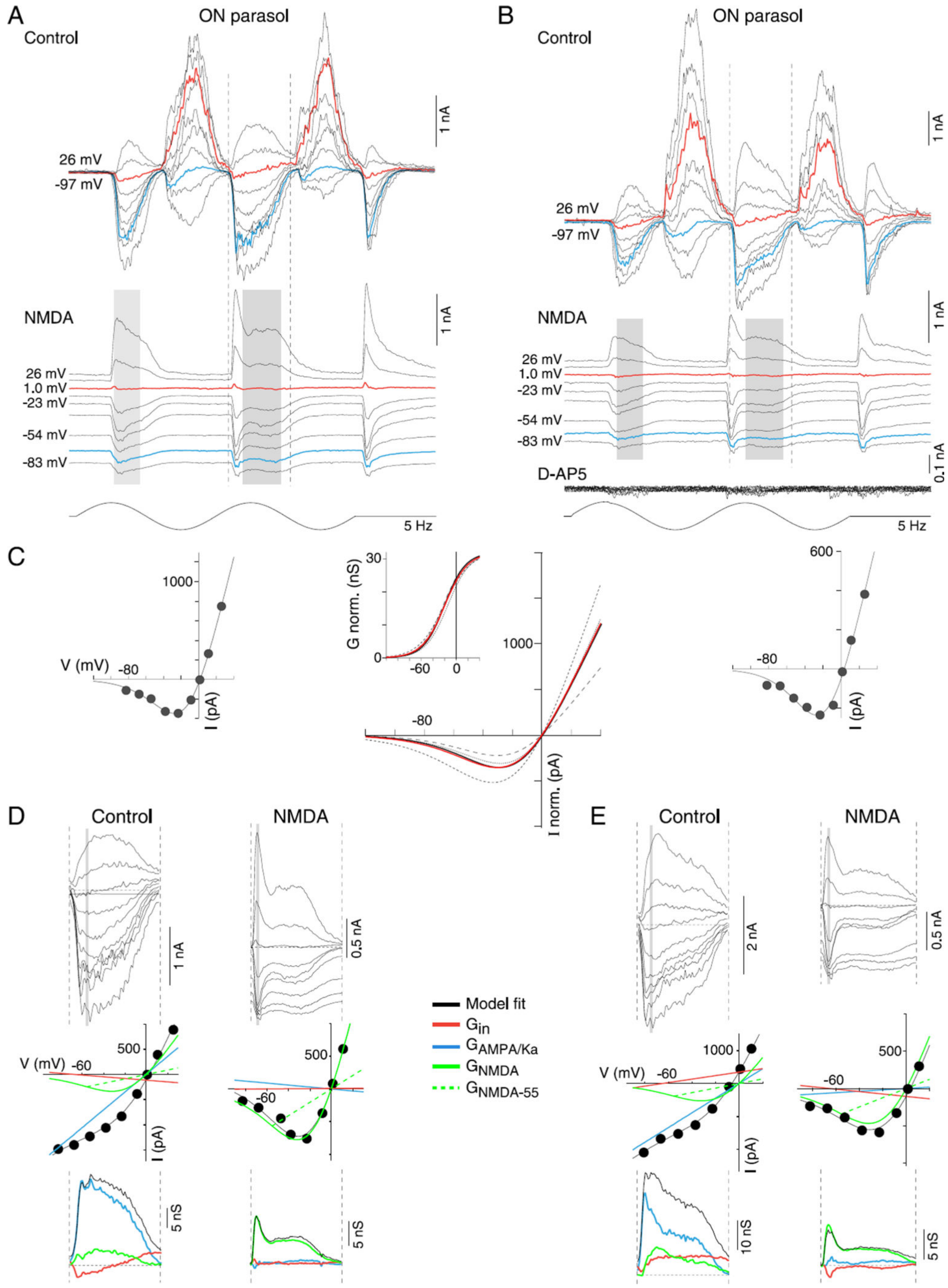

Fig. 10.

Isolation of NMDA receptor-mediated conductance in ON-center parasol cells. (**A** and **B**) Family of light-evoked synaptic currents (stimulus as in Fig. 9) from two ON-center parasol cells before (top current families, control, **A, B**), and after (lower current families, NMDA) the combined application of AMPA/kainate glutamate receptor antagonists NBQX (10 μM) and UBP 310 (10 μM) and the $GABA_A$, $GABA_C$, and glycine receptor antagonists (GABAzine, 5 μM; TPMPA, 50 μM, and strychnine, 1 μM, respectively). NMDA receptor-mediated postsynaptic currents were abolished with additional application of NMDA receptor antagonist D-AP5 (50 μM; lower traces in B, D-AP5). (**C**) *I*–*V* plots on left and right show mean *I* –*V* relationship for NMDA-mediated currents over the time indicated by the gray shading in (**A** and **B**) (*I*–*V* plots generated at 1-ms intervals) for each of the ON parasol cells; the line fit to this data describes the voltage dependence of the NMDA conductance (as in Fig. 9; see Materials and methods, eqn. 1). Middle *I*–*V* plot in **C** shows isolated mean NMDA *I*–*V* curves for four ON cells (black solid and dotted lines), normalized by their NMDA-mediated conductances. The red line plots the *I*–*V* with the mean fit parameters for K_{Mg} (3.3 mM ± 0.6; error bars ± S.D.) and V_{δ} (19.5 ± 1.7 mV; error bars ± S.D.). The inset to the middle panel plots NMDA conductance (nS) normalized to 30 nS as a function of physiological voltage (*V*) for each of the *I*–*V*s (black solid and dotted lines) and the average (red line). For this dataset, half maximal NMDA conductance = −20 m V. (**D** and **E**) Application of the NMDA conductance model shown in **C** to resolve AMPA/Ka and NMDA conductances during the excitatory phase of the control ON cell light-evoked currents shown in (**A** and **B**). (**D**) Top, family of synaptic currents from (**A**) for control and NMDA currents across time points indicated by the corresponding vertical dotted lines in (**A**). Middle, *I*–*V* relationship at time point indicated by the gray vertical bar shown for the control and NMDA currents; the black line is the fit of a model (see Materials and methods for details) that sums a linear inhibitory (red line), excitatory (blue line), and nonlinear NMDA *I*–*V* relationship (green lines). Green dotted lines indicate NMDA chord conductance at −55 mV. Bottom, total excitatory (black line), AMPA/Ka, ($G_{\mathrm{AMPA/Ka}}$ blue lines), NMDA ($G_{\mathrm{NMDA\text{-}55}}$, green lines), and total inhibitory (G_{in}, red lines) conductances calculated over time course bounded by the dotted lines in (**A**). (**E**) Current families, *I*–*V* relationships and conductances as described for (**D**), but applied to control and NMDA receptor-mediated current for ON cell shown in (**B**).

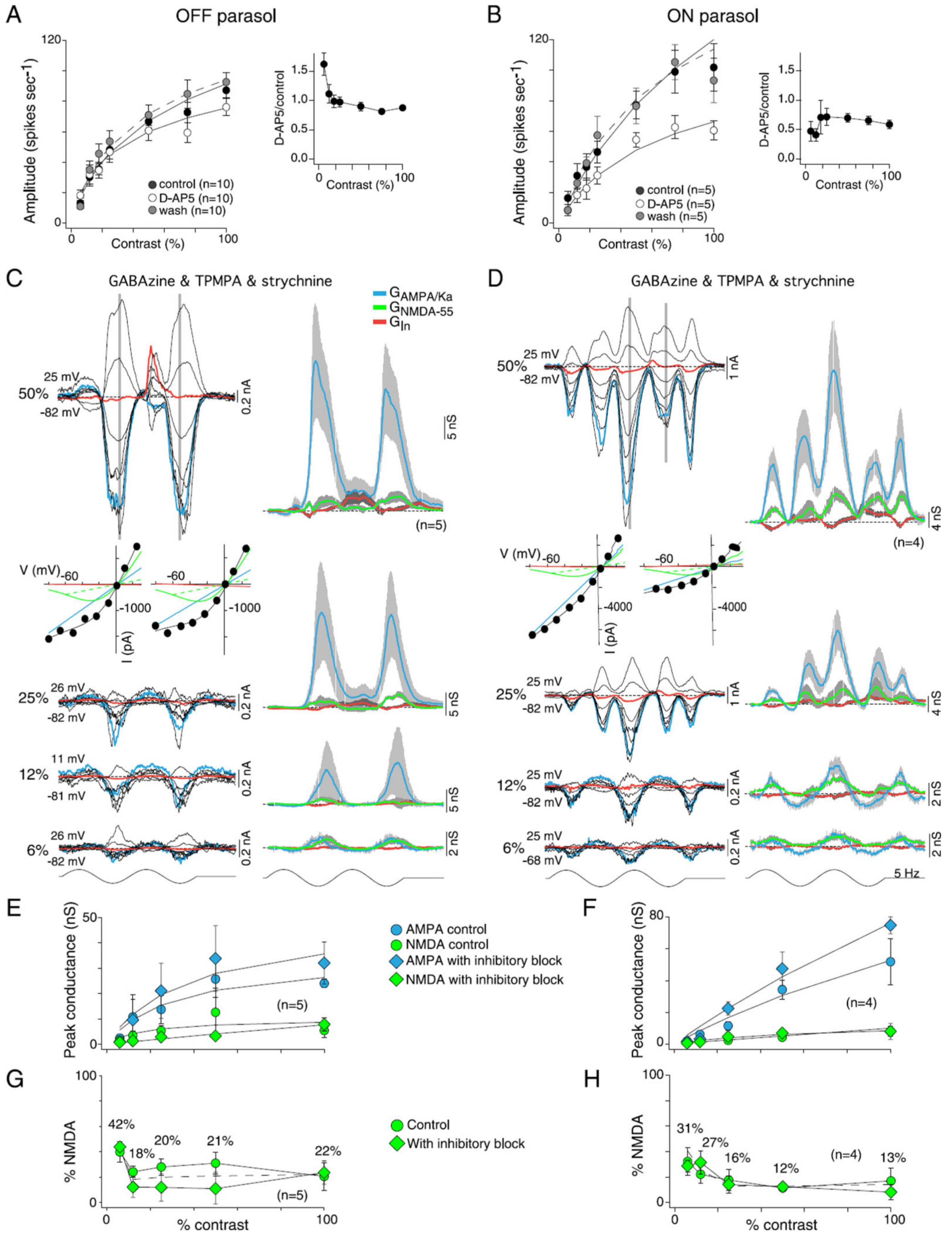

Fig. 11.

Contribution of NMDA receptors to OFF and ON parasol cells contrast sensitivity. (**A** and **B**) Effect of D-AP5 (50 μM), a selective NMDA receptor antagonist, on spike discharge in response to variation in stimulus contrast (1-mm field diameter) for OFF (**A**) and ON (**B**) parasol cells. Plots show spike response amplitude as a function of contrast for control (solid circles), D-AP5 application (open circles) and wash of D-AP5 (gray circles). Solid lines are Naka–Rushton fits (OFF control s_e = 0.8, D-AP5 s_e = 0.5, and wash s_e = 1.8; ON control s_e = 2.1, D-AP5 s_e = 1.9, and wash s_e = 3.8). Contrast gain values were not significantly altered by D-AP5 in OFF (control 3.6 ± 1.0, D-AP5 4.7 ± 1.1, and wash 3.1 ± 0.4) or ON cells (control 2.8 ± 0.5, D-AP5 2.1 ± 0.4, and wash 3.1 ± 0.4). Inset plots to the right of (**A** and **B**) show fractional change in spike rate relative to control values; OFF cells showed a smaller reduction in spike rate than ON cells and also showed a paradoxical increase in spike rate relative to control at the lowest stimulus contrasts. (**C** and **D**) Resolution of AMPA/Ka and NMDA conductances at 6, 12, 25, and 50% stimulus contrast during the block of synaptic inhibition ($\mathrm{GABA_A}$, $\mathrm{GABA_C}$, and glycine receptor block as described in Fig. 5 and 6) for OFF (**B**) and ON (**F**) parasol cells. Families of light-evoked post-synaptic currents shown on the left; derived AMPA/Ka, NMDA and inhibitory conductances shown on the right using the model described in Fig. 10 (see also Materials and methods); *I–V* plots for the 50% responses shown below current traces. (**E** and **F**) Plots of peak $G_{\mathrm{AMPA/Ka}}$ and $G_{\mathrm{NMDA\text{-}55}}$ calculated from control data (circles) and data collected after the block of synaptic inhibition (diamonds) as a function of contrast for OFF (**C**) and ON (**G**) parasol cells. Solid lines are Naka–Rushton fits (OFF cells: control AMPA $s_{\boldsymbol{e}} = 1.4$ and NMDA $s_{\boldsymbol{e}} = 1.4$, and inhibitory block AMPA $s_{\boldsymbol{e}} = 2.0$ and NMDA $s_{\boldsymbol{e}} < 0.3$; ON cells: control AMPA $s_{\boldsymbol{e}} = 1.1$ and NMDA $s_{\boldsymbol{e}} = 0.2$ and inhibitory block AMPA $s_{\boldsymbol{e}} = 2.2$ and NMDA $s_{\boldsymbol{e}} = 0.2$). $G_{\mathrm{AMPA/Ka}}$ shows steep contrast gain and saturation (OFF cells: contrast gain was 1.6 ± 0.9 for control and 1.3 ± 0.7 with inhibition blocked; ON cells: contrast gain was 0.7 ± 0.1 for control and 1.2 ± 0.2 with inhibition blocked). $G_{\mathrm{NMDA\text{-}55}}$ shows a shallow contrast gain without saturation (OFF cells: contrast gain was 0.5 ± 0.2 for control and 0.2 ± 0.0 with inhibition blocked; ON cells: contrast gain was 0.2 ± 0.0 for control and 0.3 ± 0.1 with inhibition blocked). The block of synaptic inhibition increases $G_{\mathrm{AMPA/Ka}}$ conductance but has no significant effect on the G_{NMDA}. (**G** and **H**) Plot of percentage $G_{\mathrm{NMDA\text{-}55}}$ [peak NMDA conductance/(peak total excitatory conductance + peak NMDA conductance)] as a function of contrast for OFF (**G**) and ON (**H**) cells calculated from control data (circles) and data collected after the block of inhibition (diamonds). The dotted line indicates the average. As stimulus contrast decreases, the NMDA contribution increases.

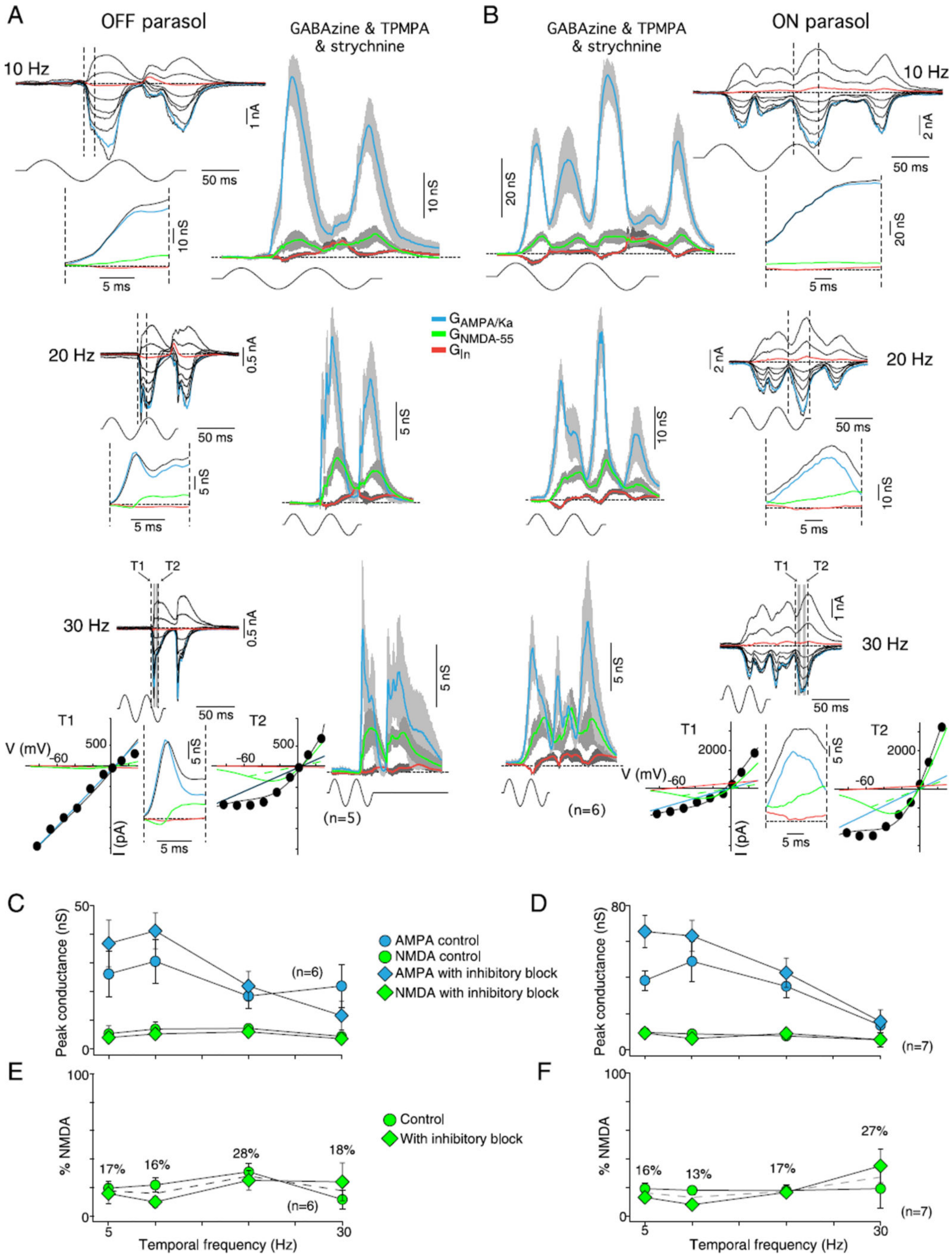

Fig. 12.

Effect of stimulus temporal frequency on AMPA/kainate and NMDA conductances in OFF and ON parasol cells. (**A** and **B**) Synaptic current families and derived $G_{\mathrm{AMPA/Ka}}$ and $G_{\mathrm{NMDA\text{-}55}}$ (conventions as in Fig. 11) for OFF (**A**) and ON (**B**) parasol cells at 10 Hz (top), 20 Hz (middle), and 30 Hz (bottom) stimulus temporal frequencies (50 and 100% stimulus contrast, 1-mm stimulus field diameter; effective quanta ~1.1×10^5 photons/s/μm^2) after application of GABA$_A$ (GABAzine, 5 μM) and GABA$_C$ (TPMPA, 50 μM), and glycine (strychnine, 1 μM) receptor antagonists. Insets below each current family show the

$G_{\mathrm{AMPA/Ka}}$ and $G_{\mathrm{NMDA\text{-}55}}$ over the stimulus-evoked conductance change indicated by the dotted lines in current traces. At 20 and 30 Hz, the OFF cells clearly show a pure $G_{\mathrm{AMPA/Ka}}$ fast transient and delayed smaller G_{NMDA}, as illustrated by the *I–V* plots either side of the 30-Hz conductances, respectively. *I–V* time points (T1 and T2) are indicated by gray boxes in the 30-Hz current traces. The frequency doubling makes it difficult to see the distinction in the ON cells. (**C** and **D**) Plots of peak $G_{\mathrm{AMPA/Ka}}$ and G_{NMDA} at four stimulus temporal frequencies for OFF (**C**) and ON (**D**) parasol cells calculated from control data (circles) and data collected after the block of inhibition (diamonds). The larger $G_{\mathrm{AMPA/Ka}}$ peaks at mid-temporal frequencies and declines at higher frequencies, ~47% decrease for the OFF parasols (16% drop for control *vs*. 68% for inhibitory block) and ~72% drop for the ON parasols (65% drop for control *vs*. 76% for inhibitory block) mirroring the temporal frequency tuning observed in the ON and OFF cell spike discharge (Figs. 7A and 8A). By contrast, G_{NMDA} remains small and unchanged (6 ± 1 nS for OFF cells and 8 ± 1 nS for ON cells) for both control and inhibitory block conditions. (**E** and **F**) Plots of percentage $G_{\mathrm{NMDA\text{-}55}}$ [peak NMDA conductance/(peak total excitatory conductance + peak NMDA conductance)] as a function of temporal frequency for OFF (**E**) and ON (**F**) cells calculated from control data (circles) and data collected after the block of inhibition (diamonds). G_{NMDA} contributed on average ~18% for both control and inhibitory block conditions for both OFF (20 ± 3%) and ON parasol cells (15 ± 1%). The dotted line indicates the average.